Journal Pre-proof

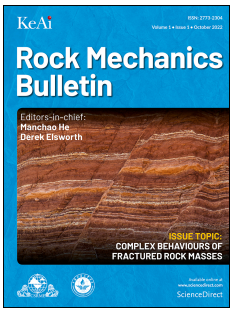

Research on the effect of surface retaining elements on the dynamic load resistance of bolted rock

Hao Feng, Lishuai Jiang, Qingjia Niu, Chunang Li, Atsushi Sainoki

PII: S2773-2304(25)00041-1

DOI: https://doi.org/10.1016/j.rockmb.2025.100214

Reference: ROCKMB 100214

To appear in: *Rock Mechanics Bulletin*

Received Date: 26 February 2025

Revised Date: 18 April 2025

Accepted Date: 17 May 2025

Please cite this article as: Feng, H., Jiang, L., Niu, Q., Li, C., Sainoki, A., Research on the effect of surface retaining elements on the dynamic load resistance of bolted rock, *Rock Mechanics Bulletin*, https://doi.org/10.1016/j.rockmb.2025.100214.

Research on the effect of surface retaining elements on the dynamic load resistance of bolted rock

Hao Feng[a,b], Lishuai Jiang[a,*], Qingjia Niu[a], Chunang Li[a], Atsushi Sainoki[c]

[a] State Key Laboratory of Mining Disaster Prevention and Control, Shandong University of Science and Technology, Qingdao 266590, China

[b] State Key Laboratory of Intelligent Deep Metal Mining and Equipment, Northeastern University, Shenyang 110004, China

[c] Faculty of Advanced Science and Technology, Kumamoto University, Kumamoto,860-8555, Japan

Abstract

The failure of support systems in deep coal mine roadways is a critical issue that hinders the development of deep coal resources. As a critical support element, the surface retaining element (SRE) plays a more prominent role in deep conditions. A comprehensive investigation into the anti-impact mechanism of an SRE on bolted surrounding rock under a dynamic load is greatly needed. In this study, split Hopkinson pressure bar (SHPB) tests were conducted to investigate the strengthening effect of different SRE areas on the mechanical properties of bolted specimens under dynamic and static loading. Moreover, the reinforcement effect of the SRE on the surrounding rock under various dynamic loadings was examined by FLAC3D. The results indicate that increasing the SRE area enhances the overall mechanical properties of the bolted specimens under combined dynamic and static loading conditions. By constructing an engineering-scale roadway numerical model, the impact of the SRE area on the amount of roof subsidence increases with increasing dynamic loading. The research findings enrich the study of the bearing capacity of SREs on bolted surrounding rock and provide a theoretical basis for controlling the surrounding rock in deep dynamic load roadways.

Key words: Surface retaining element; Dynamic loading; Bolted rock; Dynamic mechanical properties

1. Introduction

Ensuring stable roadways in underground coal mines is crucial for safe and efficient mining. Unlike other underground engineering fields (e.g., metal mining and tunneling), coal mine ground control is more challenging due to weak, fractured rock conditions, ongoing geotechnical disruptions (longwall mining, strata collapse, fault-slip), and budget constraints (Kang, 2023; Xie, 2019). With

the depletion of shallow mineral resources, deep mining has become inevitable, bringing various challenges, including high stress and strong dynamic loads, and even causing rock burst accidents under severe conditions.

At present, as the dominant supporting method for underground coal mines, surface retaining elements (SREs), such as plates, straps, and wire meshes, are indispensable in addition to rock and cable bolts (Dan, 2019). In this system, SREs play a vital role in integrating various support elements, maintaining the integrity of the surrounding rock, and transferring loads between bolts and the surrounding rocks (Li, 2017). Unlike shallow roadways, deep roadways are exposed to complex stress environments and frequent dynamic loads. As a result, a high-performance support system is needed, which highlights the function of SREs in maintaining stability and dissipating energy (Geobrugg, 2013).

In previous studies, the mechanical characteristics of rock support system SREs under dynamic load conditions have been investigated. For example, He (2021) utilized a drop hammer impact testing device to analyze the mechanical response of a plate and other SREs under impact loads. Villaescusa (2015) conducted static and dynamic loading tests on various metal meshes and plates with different material properties and sizes to investigate the support and bearing capacity of different SREs. Fu (2019) conducted mechanical property tests on conventional metal meshes using a self-developed testing apparatus. The tests were performed under both static and dynamic loading conditions to determine the stress and deformation characteristics of the metal meshes under various loading conditions. It is important to note that the bearing capacity of a rock support system under real engineering conditions, such as rock bursts and dynamic ground pressure, depends on the proper matching and combination of various support elements rather than a simple sum of the individual elements (Stacey, 2011). Designing dynamic support systems necessitates both practical experience and comprehensive experimental testing to assess their performance, especially under dynamic loading conditions (Hadjigeorgiou, 2011). To achieve this goal, Geobrugg (2013) utilized a large-scale testing system, the Western Australian School of Mines (WASM) test facility, to simulate rock burst testing of a support system consisting of bolts and high-strength metal mesh. Their investigation aimed to explore the energy-absorbing characteristics of the system and quantify its suitability for impact loading. Similarly, Louchnikov (2017) investigated the design process of roadway support under dynamic ground pressure in mining areas. These researchers analyzed the anti-impact ability

of different types of bolts and SREs from the perspectives of energy absorption and yielding.

Previous studies have mainly focused on the mechanical properties of the SRE itself. It is well accepted that the surrounding rock and support elements become a comprehensive system with mechanical interaction by rock bolting. Due to the heterogeneity and variability of surrounding rock, systematic investigations through in-situ tests remain challenging. Split Hopkinson Pressure Bar (SHPB) tests, as a high strain-rate impact methodology, serve as crucial means for evaluating rock responses under dynamic loading. Conducting rock dynamics experiments through physical modeling based on material characteristics facilitates the analysis of surrounding rock system interactions (Li, 2020). Feng et al. (2022a, 2022b) performed static-dynamic coupled loading tests on rocks containing non-coplanar and conjugate flaws, providing critical references for stability assessment and support design in rock engineering. Qiu (2025) investigated asynchronous deformation between bolts and rock through dynamic uniaxial compression tests on specimens with varying anchoring angles. Fan (2024) examined dynamic mechanical properties of bolted rocks, revealing the enhanced support efficiency of bolts in fractured rock masses under dynamic disturbances. Wu (2024) conducted dynamic tests on sand-powder 3D printed specimens with varying bolted lengths, validating their mechanical similarity to coal specimens and revealing the dynamic failure characteristics of bolted specimens.

Although existing studies have achieved meaningful progress, most scholars investigating bolt-supported structures have primarily focused on individual bolts or bolted rock masses, neglecting the structural characteristics of SRE. In other words, when the dynamic stress wave in the rock layer acts on the bolted surrounding rock of the deep roadway, the influence of SREs on the overall mechanical behavior of bolted rock masses remains insufficiently studied. In this study, a combination of specimen-scale laboratory tests and engineering-scale numerical simulations was used to analyze the reinforcement effect of SREs on the impact resistance and bearing capacity of bolted specimens under dynamic loading. The SHPB test system is used to perform impact dynamic loading tests on bolted specimens with different SREs. Additionally, numerical models of roadway support with different SRE areas are constructed to explore the control effect of SREs on the surrounding rock under different dynamic loadings. The findings of this study can provide a reference for the support design of deep coal mine roadways.

2. SHPB test of bolted specimens with different SRE areas

2.1 Test preparation and scheme

2.1.1 Specimen preparation

Natural rock's inherent heterogeneity often leads to inconsistent results in repeated tests, even when taken from the same rock body. Moreover, most mechanical tests destroy rock specimens, preventing further investigations or retesting for other properties (Wu, 2016; Gell, 2019). To address these challenges, the use of rock analogs/artificial materials began early in rock mechanical testing and is now a significant focus (Ivars, 2011; Smith, 2014). In terms of research on rock bolt reinforcement, bolted analogs made of cement (Sakurai, 2010), concrete (Ferrero, 1995) and gypsum (Xu, 2019) are widely employed.

Both natural rocks and rock analogs face a common limitation: the challenge of reproducing internal and complex defects. Methods like wire saws, water jets, and molds can only generate external and simple geometric defects (Fedrizzi, 2018). To overcome these problems, the development of 3D printing has led to recent attempts to fabricate rocks with complex defects worldwide (Tian, 2017). Recent studies have demonstrated that 3D printed sand powder analogs exhibit mechanical behavior akin to that of sandstone and other common rocks in underground mining (Jiang, 2021), as illustrated in Fig. 1 and summarized in Table 1. By investigating the strength in compression, tension and crack propagation, sand-powder 3D printing has been considered a promising technique for creating rock analogs (Tian, 2017; Primkulov, 2017; Vogler, 2017).

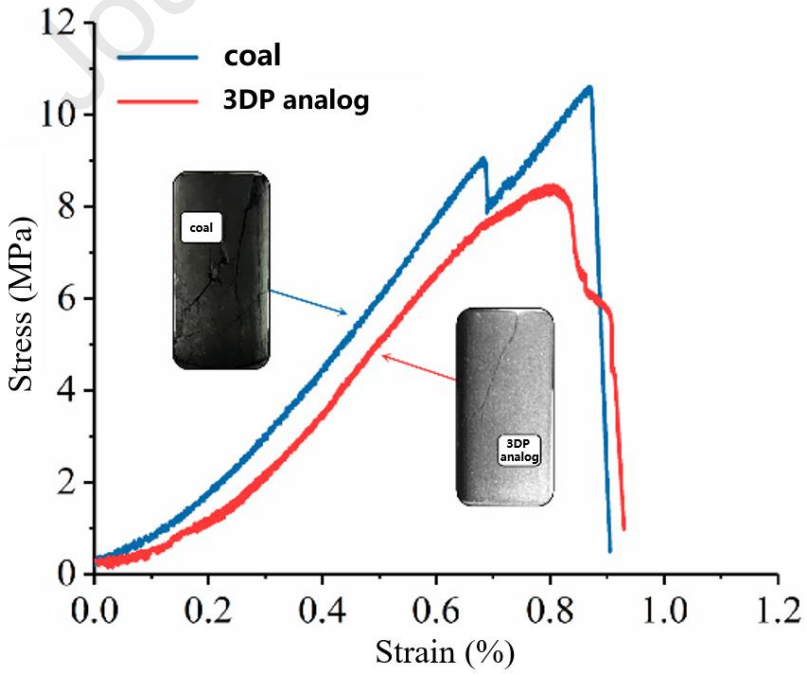

Figure 1. Stress-strain curve of coal specimen and 3D printing specimen under uniaxial

111 compression.

112 **Table 1** Mechanical parameters of 3D printing specimen and coal specimen.

Type	Compressive strength (MPa)	Tensile Strength (MPa)	Friction (°)	Cohesion (MPa)	Density (kg▪m^{-3})	Modulus of elasticity (GPa)
3D printing specimen	8.46	0.53	30.79	1.15	1426	9.60
Coal specimen	10.61	0.72	31.00	1.4	1435	11.67

113 Therefore, to avoid secondary damage to the specimen by drilling the bolting borehole, sand-
114 powder 3D printing specimens were used to prepare cylindrical specimens with a diameter and height
115 of 50 mm with a premade 4 mm diameter through-hole at its center. In laboratory tests of bolted
116 specimens, selecting the appropriate bolt materials is crucial to ensure accurate results. The materials
117 chosen for this experiment closely resemble those found in actual field conditions. SUS304 steel was
118 used as the material for the bolts, and customized M4 threaded steel and M4 galvanized washers were
119 employed to simulate the bolts and SREs, respectively. The relevant mechanical parameters of these
120 materials are presented in Table 2. For the experiment, an epoxy-type binder was chosen as the
121 adhesive. To ensure geometric similarity, a ratio of 10:1 was selected and adjusted accordingly based
122 on the experimental conditions and relevant references from the literature (Zhu, 2018).

123 The specimen preparation process involves filling the binder, adding the bolt and SRE, fastening
124 the nut, and applying pretension. The detailed procedure is illustrated in Fig. 2. The bolted specimen,
125 prepared in this manner, is similar to specimens used by other researchers and meets the requirements
126 for SHPB (split Hopkinson pressure bar) testing (Qiu, 2020).

127 **Table 2** Average values of different parameters obtained at complete pore water pressure
128 dissipation.

Material	Modulus of Elasticity (GPa)	Tensile strength (MPa)
Rebar bolt	200–210	200–600
SRE	200	350–400
SUS304 steel	194	520

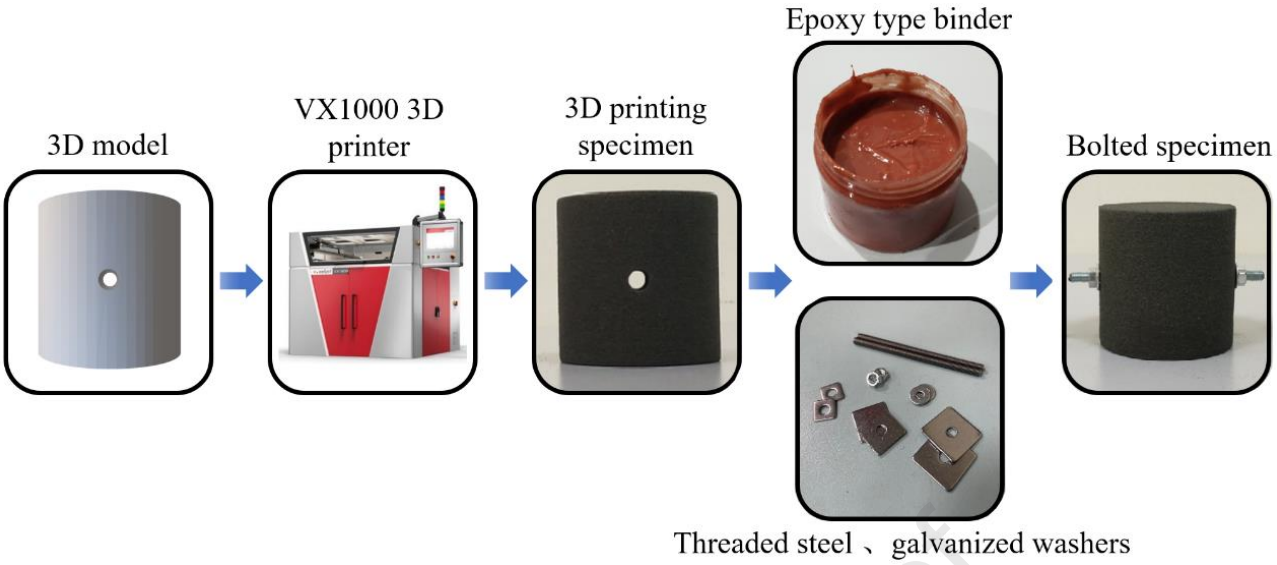

Figure 2. Preparation process of bolted specimen

2.1.2 Test design

In deep mining, the stress environment is complex, and roadways are often in an unstable state due to high stress. To investigate this phenomenon, a sample unit is extracted from one side of the roadway, and the simplified stress state is illustrated in Fig. 3(a).

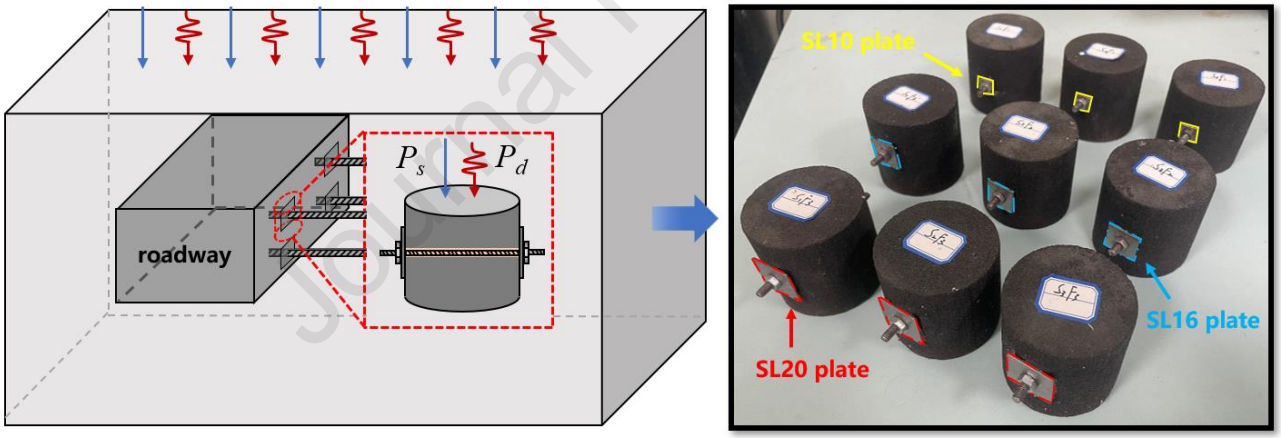

(a) Simplified stress state of the bolted rock (b) Bolted specimens with different SRE areas

Figure 3. Bolted specimens with different SREs.

When determining the axial pressure for combined dynamic and static loading, the uniaxial compression strength of the test specimen should be measured. The RLJW-2000 rock servo test system was utilized to conduct the uniaxial compression test on the specimen at a loading rate of 0.3 mm/min (Wu, 2024). Refer to the forms of bolted specimens in other papers of the research group, as shown in Fig. 4. The Modulus of Elasticity of the specimen is 5.08 MPa and the peak strength is 10.16 GPa. To account for the specimen size effect and adhere to the dynamic similarity principle, an axial

precompression of 2 MPa is set for the SHPB test. SREs with thicknesses of 0.1 mm are selected, and square plates with side lengths (SLs) of 10 mm, 16 mm, and 20 mm, representing three distinct plate areas, are labeled SL10, SL16, and SL20, respectively. The prepared specimen is illustrated in Fig. 3(b). By applying axial pressure and impact pressure, we conducted a combined loading test on bolted specimens with different SRE areas, both dynamically and statically.

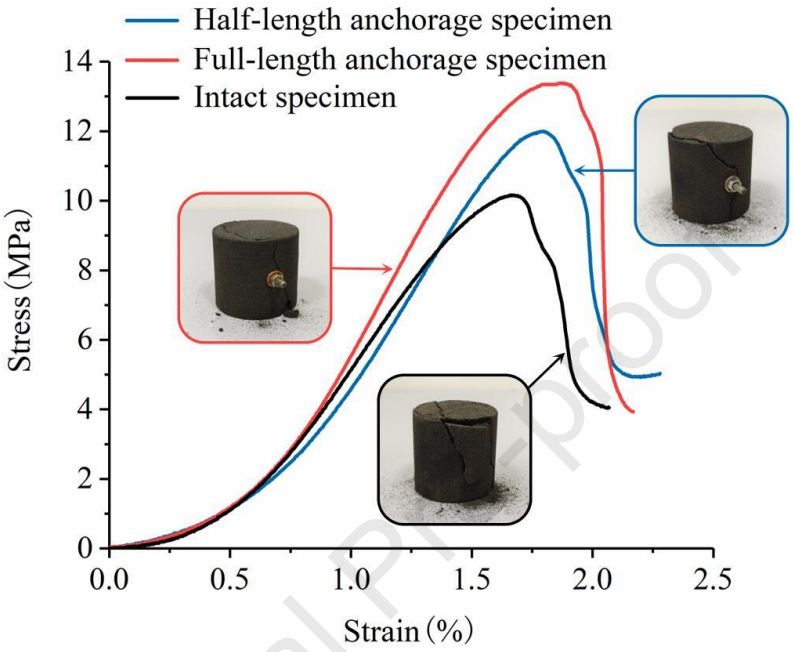

Figure 4. Stress-strain curve of specimen under uniaxial compression (Wu, 2024).

2.1.3 Test System and Program

The test was conducted with the SHPB system at Shandong University of Science and Technology. The test setup is depicted in Fig. 5. The SHPB system consists of various components, including a pneumatic loading device, an incident bar, a transmission bar, an absorption bar, a bullet, a pressure loading pump, and a data acquisition system. To ensure a high-quality waveform and achieve a smooth loading section with a sinusoidal wave, a “spindle-shaped” bullet measuring φ50 mm × 500 mm was employed. The data acquisition system consists of a high-speed camera (Vision Research/V410L) and a high-speed dynamic acquisition instrument (DH8302), which allows for the dynamic monitoring of crack evolution during the impact failure process. Before conducting the test, Vaseline is applied to both ends of the specimen, which helps reduce transverse friction and ensures proper transmission of stress waves between the incident bar and the transmission bar, ensuring good contact with the specimen.

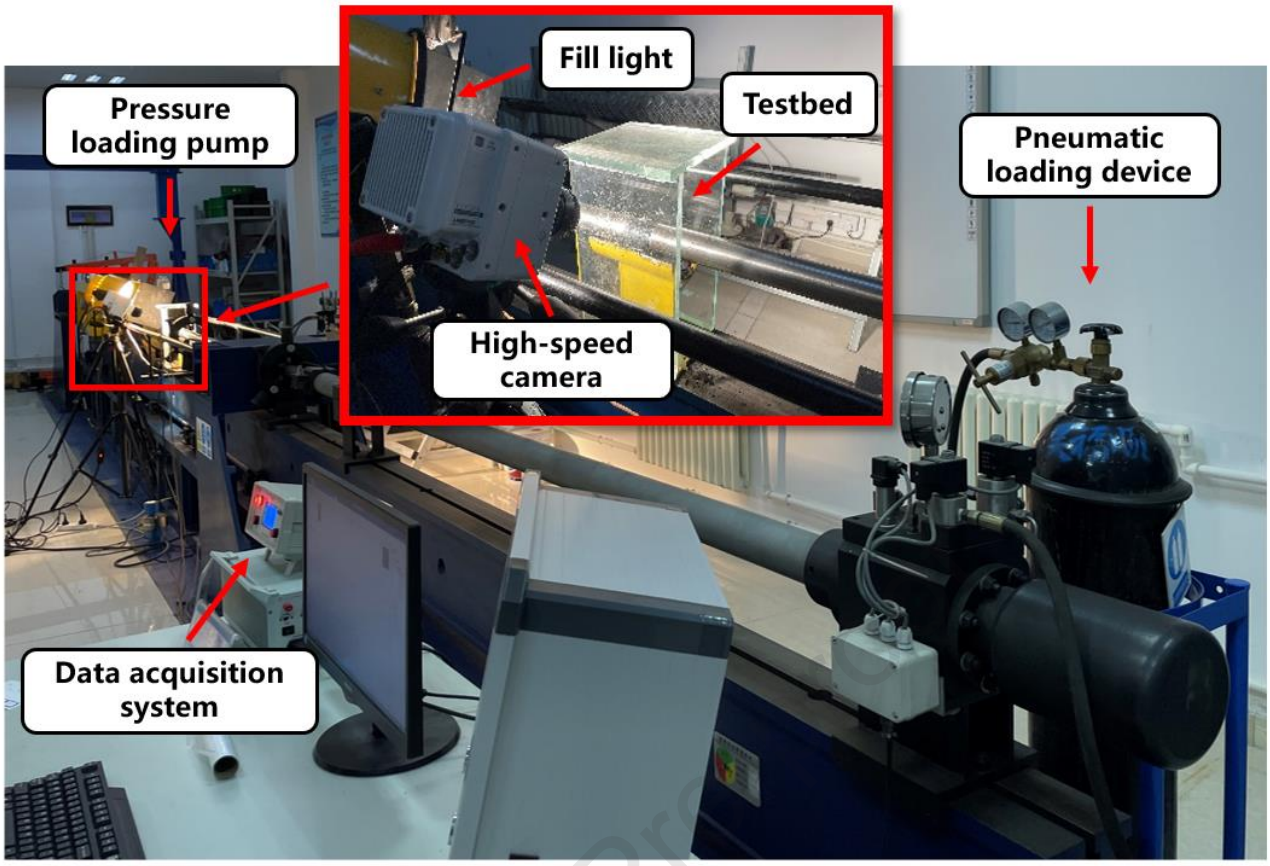

Figure 5. Split Hopkinson pressure bar test system.

The SHPB test depends on stress uniformity and one-dimensional stress wave theory. The "three-wave method" was used to measure the pulse on the incident bar and transmission bar and indirectly obtain the strain rate $\dot{\varepsilon}_s$, strain ε_s and stress σ_s of the specimen (Eqs. (1)–(3)).

$$\dot{\varepsilon}_s = \frac{C_0}{L_s}[\varepsilon_i(t) - \varepsilon_r(t) - \varepsilon_t(t)] \quad (1)$$

$$\varepsilon_s = \frac{C_0}{L_s}\int \frac{I_0}{0}[\varepsilon_i(t) - \varepsilon_r(t) - \varepsilon_t(t)]\mathrm{dt} \quad (2)$$

$$\sigma_s = \frac{EA}{2A_s}[\varepsilon_i(t) - \varepsilon_r(t) - \varepsilon_t(t)] \quad (3)$$

where C_0 represents the elastic longitudinal wave velocity of the bar, m/s; L_s is the length of the specimen, m; $\varepsilon_i(t)$, $\varepsilon_r(t)$ and $\varepsilon_t(t)$ are the time-history strains of the incident, reflected, and transmitted wave during propagation, respectively; E represents the modulus of elasticity of the bar, GPa; and A and A_s are the cross-sectional areas of the bar and the specimen, m^2, respectively.

2.2 Experimental study on the reinforcement effect of SREs

2.2.1 Analysis of the mechanical characteristics of bolted specimens under combined dynamic and static loading

Dynamic and static combined loading tests were conducted on both the intact and bolted

specimens listed in Table 3. To fulfill the testing criteria, a preimpact test was carried out to ascertain the impact velocity. Subsequently, the tests were conducted with an average impact velocity of 8.48 m/s.

Table 3 Average values of different parameters obtained at complete pore water pressure dissipation.

Remark	Type of specimens	Axial pressure (MPa)	Impact speed ($m \cdot s^{-1}$)
UB_1	Unbolted	2	6.077
UB_2			8.523
UB_3			8.498
SL10-1	Bolted with SL10 plate	2	8.234
SL10-2			8.425
SL10-3			8.558
SL16-1	Bolted with SL16 plate	2	8.555
SL16-2			8.506
SL16-3			8.481
SL20-1	Bolted with SL20 plate	2	8.496
SL20-2			8.522
SL20-3			8.490

Under the combined static and dynamic load conditions, all specimens ultimately failed. The experimental data for each specimen were analyzed, and stress–strain curves were derived for specimens with varying SRE areas, as illustrated in Fig. 6(a). The stress-strain curve of the specimens exhibits a noticeable concave downward shape, suggesting a lack of densification characteristics. This means that the specimens enter the elastic deformation stage directly upon impact, without undergoing a compaction stage. Based on the data analysis, it can be inferred that the axial pressure effectively closed the internal microcracks in the specimens. This closure was facilitated by the active diffusion of the SREs during bolt pretightening and the passive enhancement of clamping during preloading. Both processes contributed to the accelerated densification and closure of microcracks. As the strain increased, the stress within the specimens gradually peaked and then decreased, demonstrating clear overall elastic–plastic characteristics. The comparative test results indicate that the presence of bolts and SREs has a noteworthy positive impact on the dynamic strength and dynamic modulus of elasticity of the bolted specimens. In comparison to the unbolted specimen, increasing the size of the bolt and square plate results in significant improvements in the average dynamic

strength and dynamic modulus of elasticity of the SL10 specimen. Specifically, the average dynamic strength increases by 2.05 MPa (a 9.78% increase), and the dynamic modulus of elasticity increases by 0.488 GPa (a 6.90% increase). When using 16 mm and 20 mm square plates with larger SRE areas, the dynamic modulus of elasticity of the bolted specimens remains relatively unchanged, while the dynamic strength further improves. In comparison to the SL10 specimen, the average dynamic strength of the SL16 specimen increases by 2.20 MPa (an 8.46% increase), and the dynamic modulus of elasticity increases by 0.028 GPa (a 0.37% increase). Similarly, compared to SL10, the average dynamic strength of the SL20 specimen increases by 1.93 MPa (a 7.66% increase), while the dynamic modulus of elasticity increases by 0.023 GPa (a 0.30% increase).

The experimental analysis shows that, under combined static and dynamic loads, the reinforcement effect of SREs on bolted specimens is directly proportional to the SRE's surface area. However, the increase in the modulus of elasticity is relatively small. Unlike elements such as bolts, which directly exert their influence on the interior of the rock, the reinforcement effect of SREs is often more prominently manifested during the loading process. The modulus of elasticity serves as a crucial indicator for measuring a material's resistance to deformation and is closely linked to stress and strain. When subjected to low strain rate quasistatic loading conditions, the loading process of the bolted specimen allows sufficient time for the SRE to undergo uniform loading and stabilize force transmission. However, under high strain rate loading conditions, such as instantaneous impact, the specimen undergoes rapid loading that can result in immediate failure. The short duration of the loading event and the high strain rates involved can result in different behaviors and failure mechanisms compared to quasistatic loading.

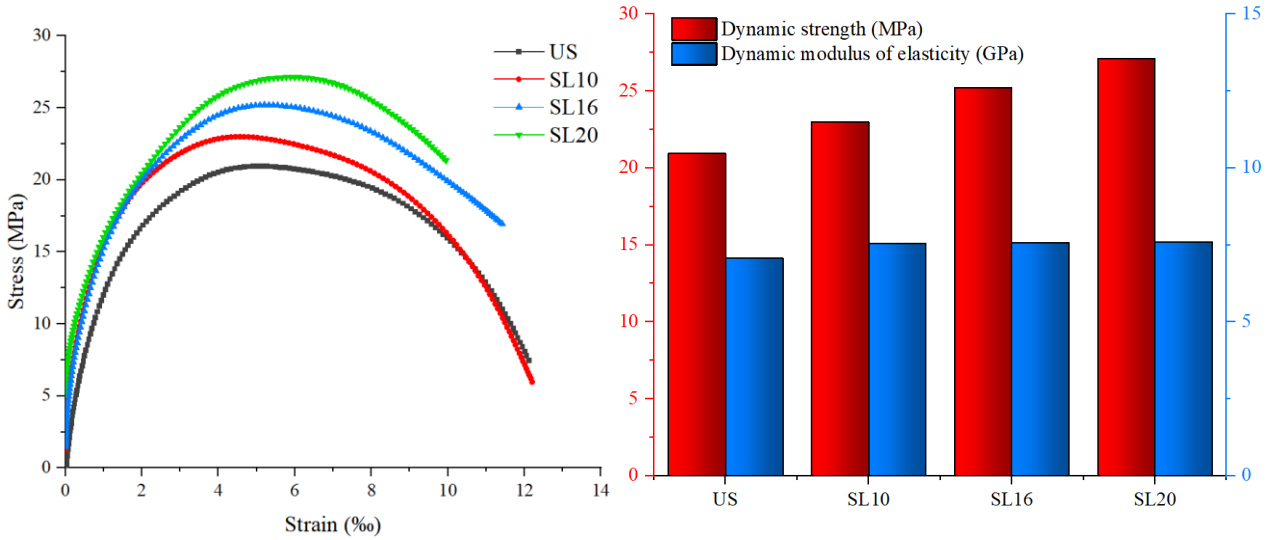

(a) Stress–strain curve (b) Dynamic strength and modulus of elasticity

Figure 6. Mechanical behaviors of bolted specimens with different SRE areas.

In the SHPB test, the impact pressure is transmitted through the specimen using stress waves, traveling from the incident bar to the transmission bar and back. Throughout this process, the elastic strain energy generated by the incident bar transforms into various forms of energy. The part of this energy absorbed by the specimen dissipates as the energy required for crack propagation, while the remaining, smaller portion dissipates in the form of heat energy (Han, 2022). The average dissipated energy of bolted specimens with different SRE areas is shown in Fig. 7. It is observed that as the SRE area increases, the dissipated energy of each specimen also increases, and there is a linear positive correlation between them. The average dissipative energies of the bolted specimens with three different SRE areas are 21.67 J, 23.46 J, and 25.48 J. These values are 9.72%, 18.78%, and 29.01% higher than the dissipative energy of the unbolted specimen. Under the lateral constraints provided by the bolt and SREs, the bolted specimen exhibits an enhanced capacity to withstand dynamic loading. Additionally, the support elements, along with the specimen, contribute to energy dissipation by absorbing a portion of the energy. This increased dissipation of stress wave energy is attributed to the combined effect of the bolt, SREs, and support elements.

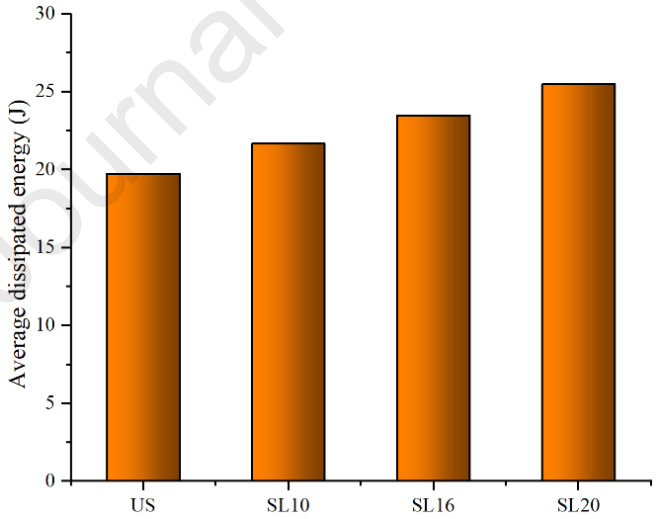

Figure 7. Average dissipated energy of bolted specimens with different SRE areas.

2.2.2 Analysis of deformation and failure characteristics of the bolted specimen under dynamic and static combined loading.

(1) Crack evolution of specimens

In this study, high-speed cameras (Vision Research/V410L) were used to capture the entire process of damage, crack development, and macroscopic failure of the bolted specimens. The camera samples at 650,000 fps with a maximum resolution of 1024 × 1024 pixels. Captured images were

processed using VIC-2D software for detailed analysis. The evolution of the principal strain for each specimen under combined dynamic and static loading was obtained and is presented in Fig. 8.

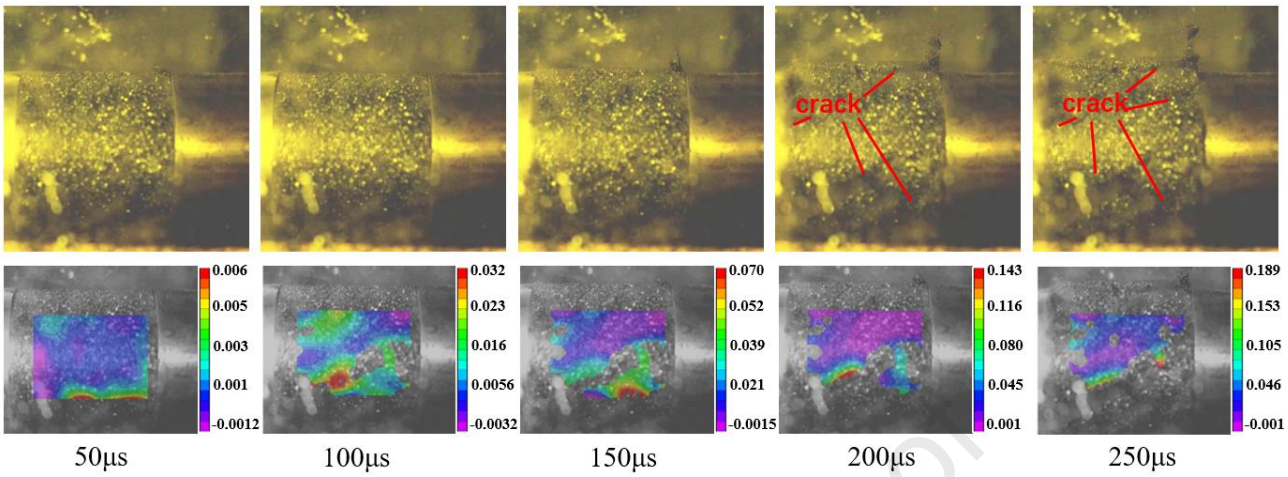

(a) Unbolted

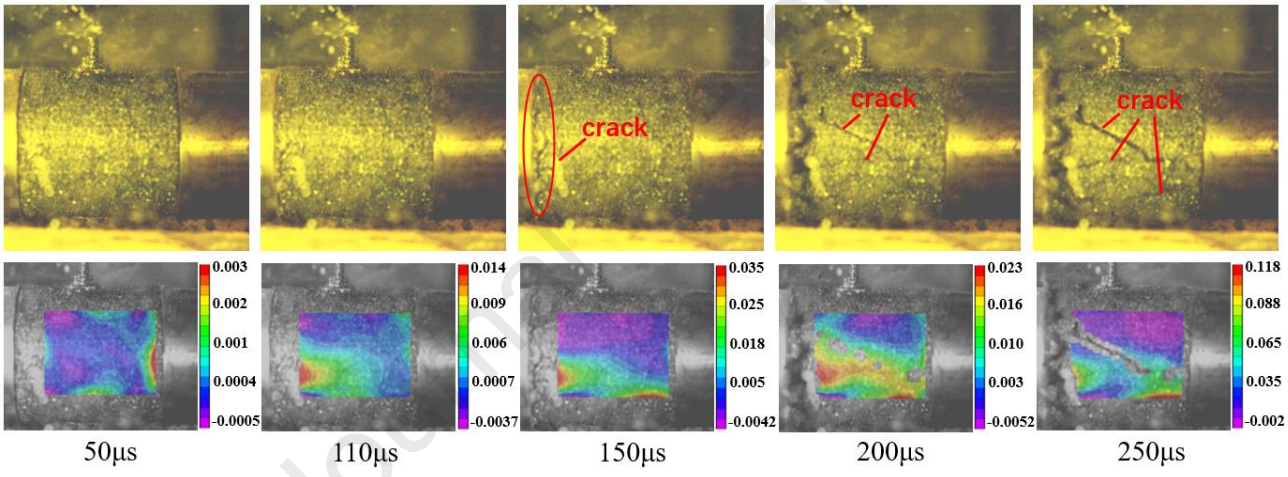

(b) Bolted with SL10 plate

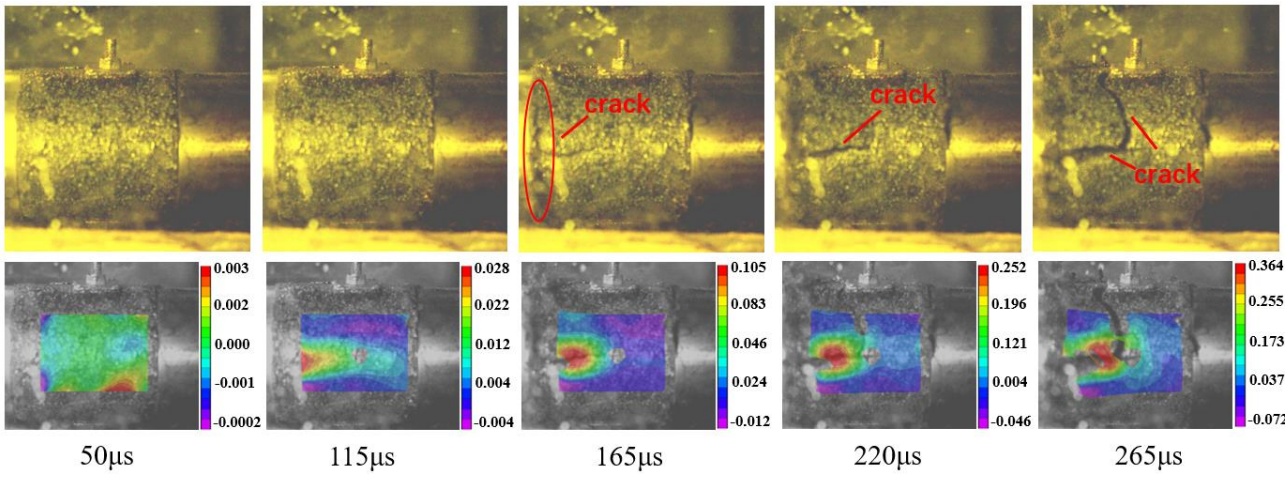

(c) Bolted with SL16 plate

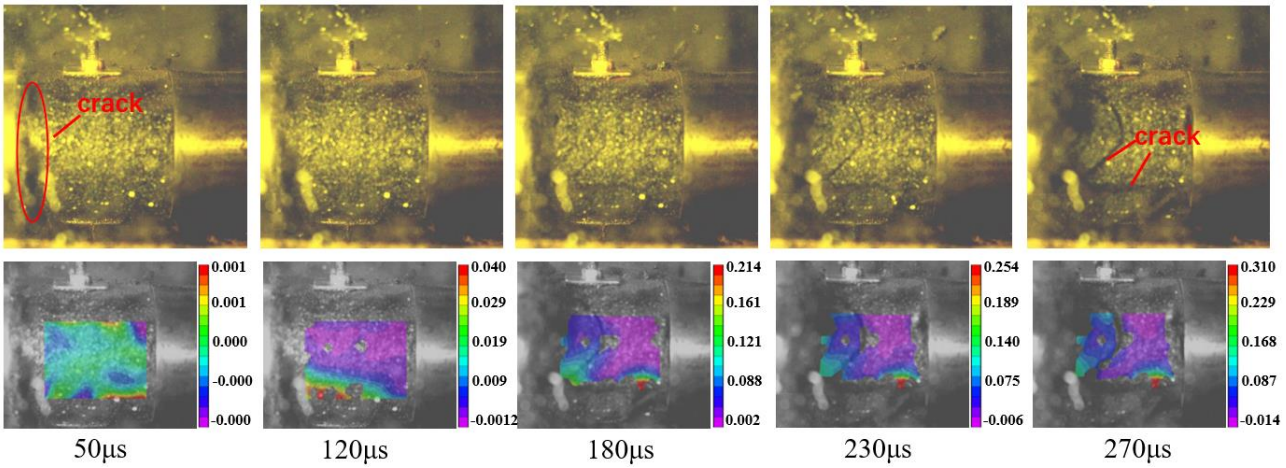

(d) Bolted with SL20 plate

Figure 8. Evolution of the principal strain of bolted specimens with different SRE areas.

From Fig. 8, it is evident that there are significant differences in the crack development and macroscopic failure patterns between the unbolted specimens and the bolted specimens with different SRE areas. In the case of unbolted specimens, the initiation position of cracks appears to be disordered and nonuniform, with multiple points of initiation. During macroscopic failure, each crack tends to be parallel to the direction of the dynamic loading, indicating a typical fracture failure pattern. On the other hand, in the bolted specimens with different SRE areas, dense cracks first emerge at the ends of the specimens where the bolts are located. Subsequently, crack initiation occurs parallel to the loading direction. Importantly, the crack initiation points are primarily situated on the nonbolting surface, and the number of cracks observed is relatively small. Indeed, the presence of rock bolts and SREs not only enhances the mechanical properties of the specimen but also contributes to its structural stability. The anchoring effect of the bolt reduces the likelihood of initial damage occurring in specific areas of the specimen, while the fastening effect of the SRE further enhances the overall stress distribution within the specimen. Under dynamic load conditions, the end face of the farther specimen from the bolt is less influenced by support elements. As a result, it is more likely to come into contact and friction with the pressure bar, leading to the generation of a hoop effect.

When comparing the principal strain of each specimen, it can be observed that crack initiation in the unbolted specimen is accompanied by multiple strain concentrations. In contrast, the location of the crack initiation point and the presence of strain concentration in the bolted specimens are similar. Based on the analysis of the crack evolution process, the macroscopic failure of the unbolted specimen is influenced by the development and closure of multiple primary and secondary cracks. In

contrast, the failure pattern of the bolted specimen is characterized by 1–2 initial cracks, which may occur under certain conditions, along with the development of secondary cracks in conjunction with the primary cracks. In terms of the final crack propagation, both the unbolted specimen and the bolted specimens with an SL10 plate exhibited lateral splitting cracks. However, in the case of bolted specimens with an SL16 and SL20 plate, transverse cracks perpendicular to the loading direction were observed. These cracks expanded along the edge of the SRE.

Surface cracks morphology of the specimens after impact was extracted and analyzed, as illustrated in Fig. 9. The bolted specimens with an SL10 plate predominantly exhibited tensile-shear hybrid cracks characterized by asymmetric X-shaped shear failure patterns (Fig. 9a). Shear cracks initiated at the specimen tips and propagated diagonally within the specimens. In contrast, the bolted specimens with SL16 and SL20 displayed localized macro-fragment spalling, typically forming conical geometries regardless of failure modes (Fig. 9b and c). The morphology of throughgoing cracks in bolted specimens was governed by the SRE area: larger SREs expanded the anchorage zone, particularly in regions proximal to the bolt ends. When the SRE area increases from SL16 to SL20, the spalling position of the fragments will change from the corner to the center of the load end, indicating that the larger area of SRE changes the effect of stress transfer and concentration. The analysis conducted demonstrates that under combined dynamic and static loading conditions, the lateral constraints provided by the SREs on the specimen are strengthened through the continuous action of dynamic stress waves. This leads to a closer cooperation in deformation between the bolt and the specimen, resulting in a change in the failure mode of the specimen. The use of a larger SRE area proves beneficial for delaying the initiation of cracks, reducing crack propagation, and enhancing the overall integrity of the specimen after impact failure.

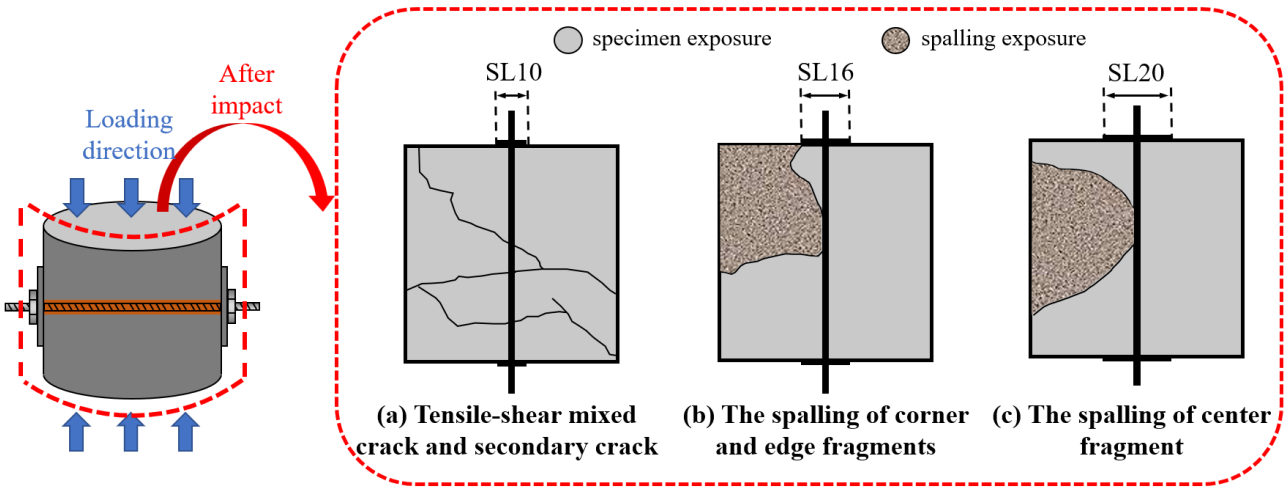

Figure 9. Surface cracks morphology of bolted specimens with SREs.

(2) Fragmentation of specimens

After impact, the specimens experienced crushing, resulting in the production of fragments with varying sizes and shapes. These fragments, along with the presence of fine particles, serve as crucial indicators for determining the bearing capacity of the samples. Furthermore, they provide essential material evidence for understanding the mechanism of SREs in bolted specimens. Figure 10 illustrates the ultimate failure of each bolted specimen under combined static and dynamic loading.

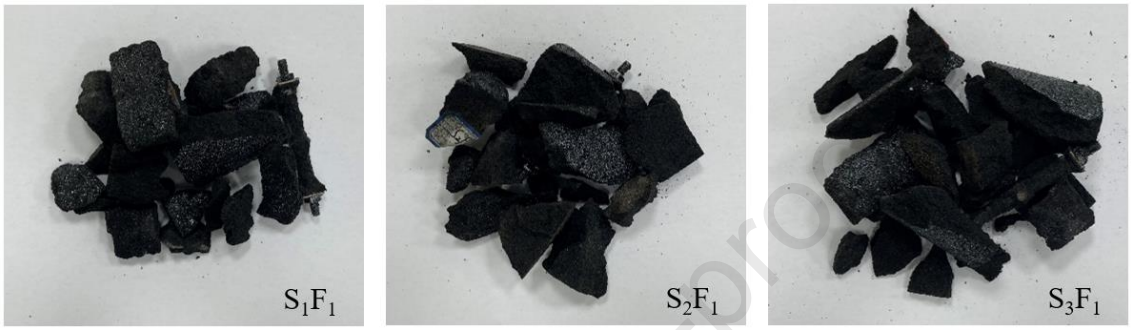

(a) Bolted with SL10 plate

(b) Bolted with SL16 plate

(c) Bolted with SL20 plate

Figure 10. Failure pattern of bolted specimens with SREs.

From Fig. 10, it is clear that the presence of SREs significantly affects the final failure mode of the specimen. When an SL10 plate is used, there is an increase in the volume of the specimen fragments after impact. However, a larger quantity of fine particles with small diameters remains in

316 the resulting fragments. When using SL16 and SL20 plates, there is an additional increase in the bulk
317 percentage of the specimens after impact. Additionally, there is a decrease in the occurrence of small-
318 diameter fine particles. Three different SRE schemes were implemented using the full-length
319 anchoring method to ensure that the bolts made solid contact with the rock and did not detach
320 completely. As the SRE area increased, there was a noticeable decrease in the overall failure rate and
321 the number of fragments generated.

322 The fragments of the specimens underwent additional sieving and weighing. Based on their size,
323 they were categorized into three grades based on lumpiness range: Grade I (1 cm > r), Grade II (2
324 cm > r ≥ 1 cm), and Grade III (r ≥ 3 cm). Through the process of sieving the fragments along their
325 longest diameter, the lumpy mass ratio was calculated for each bolted specimen after crushing. Figure
326 11 illustrates the results of the mass ratio of lumpiness for the specimens. When comparing the
327 specimen with an SL10 plate to those with SL16 and SL20 plates, the following observations can be
328 made: In the specimen with an SL16 plate, there was a 26.88% decrease in the mass proportion of
329 fragments smaller than 1 cm, a 21.78% decrease in the mass proportion of fragments smaller than 3
330 cm, and a 20.57% increase in the mass proportion of fragments larger than 3 cm. In the specimen
331 with an SL20 plate, there was a significant decrease in the mass proportion of fragments smaller than
332 1 cm by 68.5%, a decrease in the mass proportion of fragments smaller than 3 cm by 28.12%, and an
333 increase in the mass proportion of fragments larger than 3 cm by 35.00%. The results demonstrate
334 that increasing the SRE area has a significant impact on the number of fragments in various size
335 ranges. Enlarging the SRE area significantly reduces small-sized fragments and increases large-sized
336 fragments, improving the specimen's post-peak residual bearing capacity.

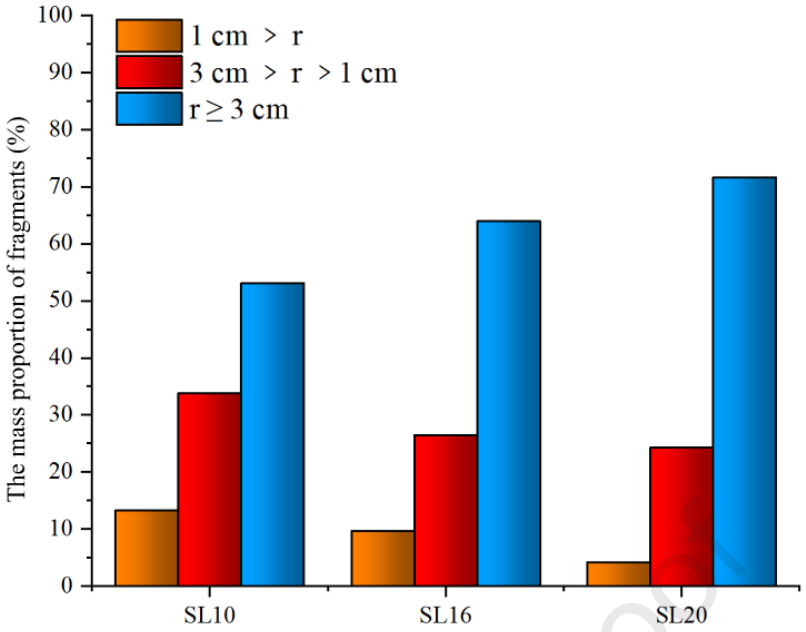

Figure 11. Mass proportion of broken bolted specimens with SREs.

Figure 12 shows the damage patterns at the contact point of the bolt, specimen, and SRE after the impact failure of the bolted specimen under different SRE areas. It can be observed that there are clear variations in the extent of anchorage within the three SRE areas. By analyzing the final bonding morphology of the specimens, we can intuitively obtain the spatial distribution of the residual anchorage range after impact failure. When using an SL10 plate, the failure surface of the bolt/anchor agent appears uneven, suggesting an irregular bonding pattern. The contact area between the bolt and the specimen is small, and a limited range of bolt control areas is observed only in the loading direction. When using the SL16 and SL20 plates, the failure surface of the bolt/anchor agent is smooth without any protrusions. The specimen is securely bonded between the bolts in a conical shape, which leads to an increased contact area and a broader range of residual anchorage. As the SRE area increases, the control range of the bolt expands, resulting in a transformation of the rock shape within this range from flat to three-dimensional. Under the influence of dynamic loading, the specimen fails as a result of the initiation, propagation, convergence, and closure of primary and secondary cracks. These cracks propagate through the specimen, ultimately leading to its ultimate failure. The anchoring effect of the bolt plays a role in restraining crack propagation and improving the bearing capacity in this process. The key to achieving this effect lies not only in the bonding of the anchor agent to the bolt and the specimen but also in the diffusion of the initial pretightening on the bolt by the SRE. Under the influence of SREs, the pretightening force of the bolt spreads out toward the periphery of the specimen. This expands the anchorage range of the bolt, in addition to the bonding provided by

the anchoring agent. The positive correlation between the SRE area and the residual anchorage range suggests that enhancing the area attribute of the SRE can effectively improve the anchoring ability of the bolt. By increasing the surface area of the SRE, the contact state between the specimen and the bolt is improved, resulting in an enhanced supporting effect of the bolt. This enhanced contact state ensures improved load transfer and distribution, ultimately enhancing the overall effectiveness of the bolt support system.

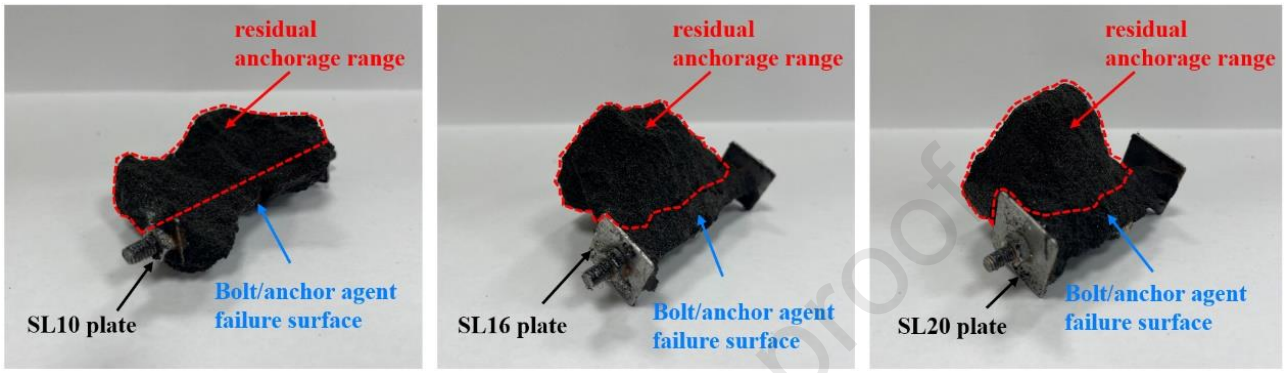

Figure 12. Failure characteristics of bolted specimens with SREs.

3. Numerical analysis of the supporting effect of the SRE on roadway surroundings under dynamic loading

While the reinforcement effect of SRE on bolted rock under dynamic loading was analyzed with experimental analysis, its performance under engineering conditions, especially in the evaluation of support response under dynamic load and combined support, require. Conducting an analysis of the supporting effect of support elements on roadway surrounding rock under laboratory conditions is challenging. This includes simulating and applying the primary rock stress field and bolt preload, assessing the degree of roadway deformation convergence, and achieving group anchor combined support of bolts and SRE. Numerical simulation is used to simulate the full cycle of roadway support process and dynamic load stress waves of different strengths, which is helpful for us to further understand the reinforcement effect of SRE under real working conditions.

In this study, we utilized FLAC3D to construct an engineering-scale numerical model of a roadway, as shown in Fig. 13(b). The model incorporates a nonlinear dynamic calculation module within the software, enabling us to analyze the supporting effect of the SRE under different dynamic loadings.

By conducting these analyses and simulations, we can gain valuable insights into the behavior and performance of the SRE in practical scenarios. This will provide a better understanding of the

potential benefits of enhancing the stability and resilience of bolted support systems in response to dynamic load conditions.

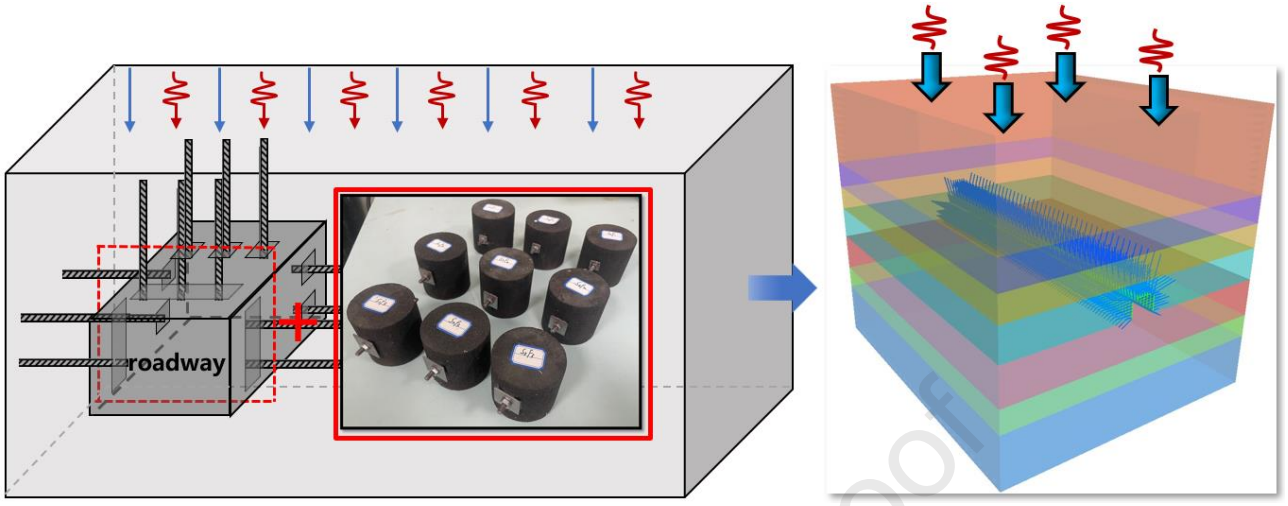

(a) Simplified stress state of the bolted roadway (b) Engineering-scale numerical model of a roadway

Figure 13. Bolted roadway with different SREs.

3.1 Model description

In this study, we constructed a three-dimensional numerical model in FLAC3D based on the actual geological conditions of a deep rock burst mine (Xu, 2021). Normal displacement constraints were applied to the bottom and peripheral boundaries to simulate far-field geological constraints. The initial stress field was calibrated based on in-situ geostress measurements, with an overburden unit weight assumption of 0.025 MN/m³. A vertical stress of 24 MPa (corresponding to a burial depth of approximately 1000 m) was applied to the top boundary, and horizontal stresses in the x- and y-directions were set to 0.75 times the vertical stress. The acceleration due to gravity was considered to be 9.8 m/s². Prior to roadway excavation simulations, multi-step iterative calculations ensured equilibrium of the initial geostress field. The mechanical parameters of the coal and rock mass used in the model are provided in Table 4. The model is defined as a strain softening model, and this model has been widely accepted for the simulation of underground coal mines (Khoshmagham, 2025).

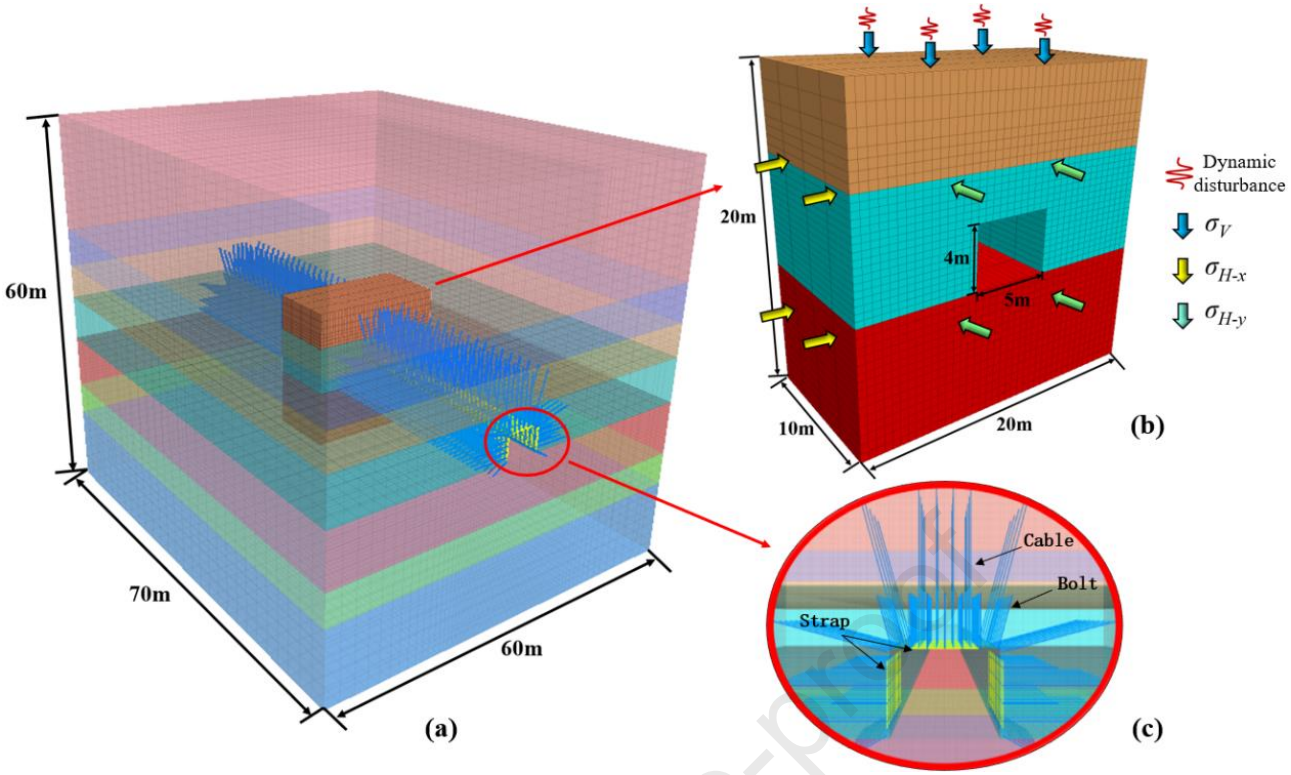

(a) Roadway (b) Monitoring section and boundary condition (c) Support scheme

Figure 14. Three-dimensional numerical model.

Table 4 Mechanical parameters of the coal and rock mass.

Lithology	Bulk modulus (GPa)	Shear modulus (GPa)	Density (kg/m^3)	Friction angle (°)	Cohesion (MPa)	Tensile strength (MPa)
fine sandstone	6.83	6.24	2700	40	3.30	4.19
argillaceous sandstone	7.22	4.15	2657	35	3.50	3.75
sandy mudstone	5.18	3.20	2724	37	2.7	2.20
coal	1.02	0.41	1651	32	1.50	0.31
sandy mudstone	5.18	3.20	2724	37	2.7	2.20
fine sandstone	6.83	6.24	2700	40	3.30	4.19
argillaceous sandstone	7.22	4.15	2657	35	3.50	3.75

In the constructed FLAC3D numerical model, a roadway is excavated at the center of the model along the bottom of the coal seam. The roadway has dimensions of 70 m in length, 5 m in width, and 4 m in height. To simulate roadway support, we used built-in structural elements such as cables and beams, which represent the actual support scheme used in field applications (see Fig. 14(c)). In

FLAC3D, beams are commonly used to simulate straps. However, reflecting the parameter of the strap area directly in the simulation can be challenging due to the limitations of structural element properties. To indirectly represent the role of the SRE area, we can adjust the horizontal value distribution under different SRE areas by increasing the length of the beam in the longitudinal direction and the moment of inertia in the transverse direction, as depicted in Fig. 15. The support elements used in the model consist of high-strength rebar bolts and steel strand wires, which are anchored using resin. W-shaped straps are used as the SRE. The mechanical parameters of the support elements are detailed in Table 5 and Table 6.

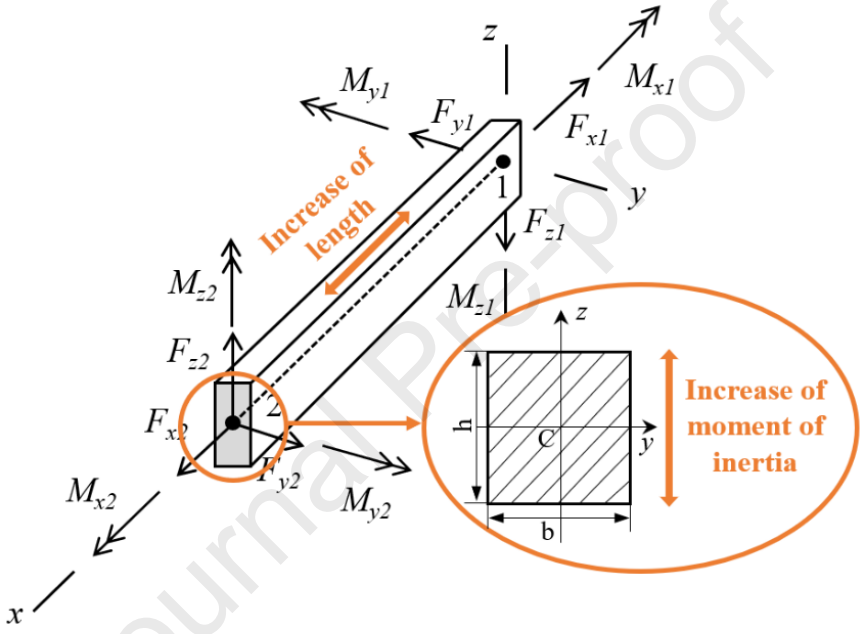

Figure 15. The embodiment of the SRE area in the beam.

Table 5 Mechanical parameters of the bolt cable.

Support scheme	Length (mm)	Anchorage length (mm)	Diameter (mm)	Pre-tightening (kN)	Tensile strength (MPa)
Bolt	2500	1250	20.0	30	335
Cable	7300/5300	2400	21.6	100	510

Table 6 Mechanical parameters of the strap.

Support scheme	Width (mm)	Thickness (mm)	Moment of inertia (mm^4)	Modulus of elasticity (GPa)	Poisson ratio
W-shaped strap	310	3	40768	206	0.3

3.2 Simulation design

In the mining environment, various dynamic events with different focal mechanisms can occur, each of which can have different effects on the stability of the roadway. However, accurately locating the source of these events can be challenging. The stress wave generated by the source undergoes multiple interferences and propagations, making it difficult to derive an analytical formula theoretically. To simulate the seismic activity caused by underground mining, we utilized an interface source and applied a sinusoidal simple harmonic wave (with a frequency of 10 Hz and a period of 0.1 s) to the top of the model. The stress waves of dynamic loading will be applied after roadway support and balance. The model boundary was set as a viscous boundary to prevent the reflection of seismic waves. A local damping coefficient of 5% was selected. This setup allows us to effectively simulate the stress waves of dynamic loading under various source intensities. The detailed simulation scheme, including the different peak velocity (*PPV*) settings, is provided in Table 7.

Table 7 Design scheme of the experiments.

Scheme	Bolt spacing (mm)	Bolt length (mm)	Strap area (m^2)	*PPV* ($m \cdot s^{-1}$)
1	1200	3500	0.744	0
2	1200	3500	0.930	0
3	1200	3500	1.116	0
4	1200	3500	0.744	0.5
5	1200	3500	0.930	0.5
6	1200	3500	1.116	0.5
7	1200	3500	0.744	1.0
8	1200	3500	0.930	1.0
9	1200	3500	1.116	1.0
10	1200	3500	0.744	1.5
11	1200	3500	0.930	1.5
12	1200	3500	1.116	1.5

3.3 Simulation results

3.3.1 Influence of the SRE area on the deformation of the surrounding rock under dynamic loading

The instability of the roadway is primarily characterized by the instability of its spatial structure. After implementing support elements such as bolts, one of the most intuitive and effective ways to assess the support effect is by examining the deformation characteristics of the bolted rock (Li, 2021). The deformation of the roadway in the monitoring section was extracted under different strap areas and dynamic loadings. Since the simulation involves a variety of working conditions, in order to

clearly convey the evolution, representative test groups are selected for illustration. Figures 16 (a) and (b) are roof vertical displacement distribution of different SRE areas under conditions of no dynamic load and high dynamic load, respectively. The study reveals a direct relationship between roof subsidence and dynamic loading. An increase in dynamic loading leads to higher roof subsidence. Additionally, a significant negative correlation is observed between roof subsidence and the strap area, regardless of the magnitude of the dynamic loading. In order to further quantitatively characterize the influence of strap area and *PPV* on roof deformation, the maximum subsidence of roof under different working conditions was extracted, as shown in Fig. 17. When the strap area is 0.744 m^2 and the *PPV* increases from 0 m/s to 1.5 m/s, the roof subsidence also increases from 251.27 mm to 446.15 mm. This indicates a significant rise of 194.88 mm. Similarly, with a strap area of 1.116 m^2, the increase in *PPV* from 0 m/s to 1.5 m/s results in a rise in roof subsidence from 192.93 mm to 363.25 mm, indicating an increase of 170.32 mm. The results reveal a consistent trend of roof subsidence with varying strength of dynamic loading across the three schemes. However, as the dynamic loading increases, the impact of the SRE area on roof subsidence becomes more significant. In the presence of high dynamic loading, increasing the SRE area leads to a more significant reduction in roof deformation compared to the situation with low dynamic loading.

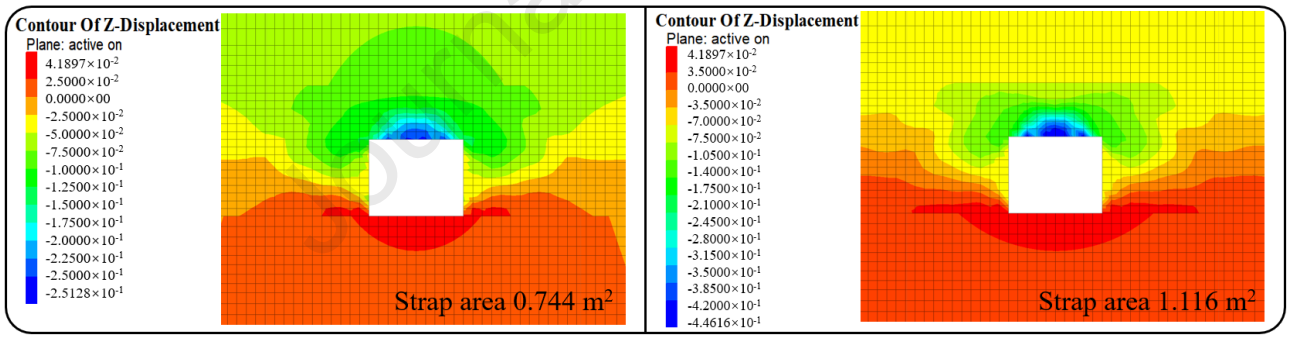

(a) PPV=0 m/s

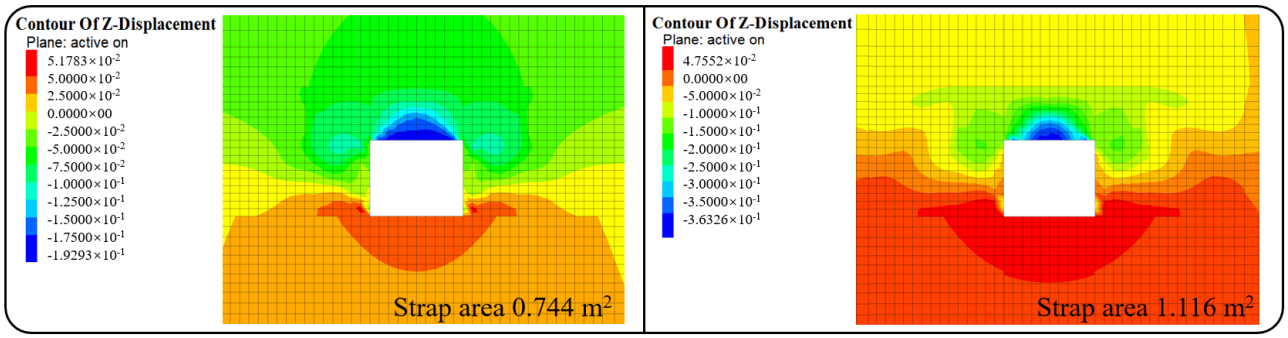

(b) PPV=1.5 m/s

Figure 16. Roof vertical displacement distribution under different strap areas and dynamic loadings.

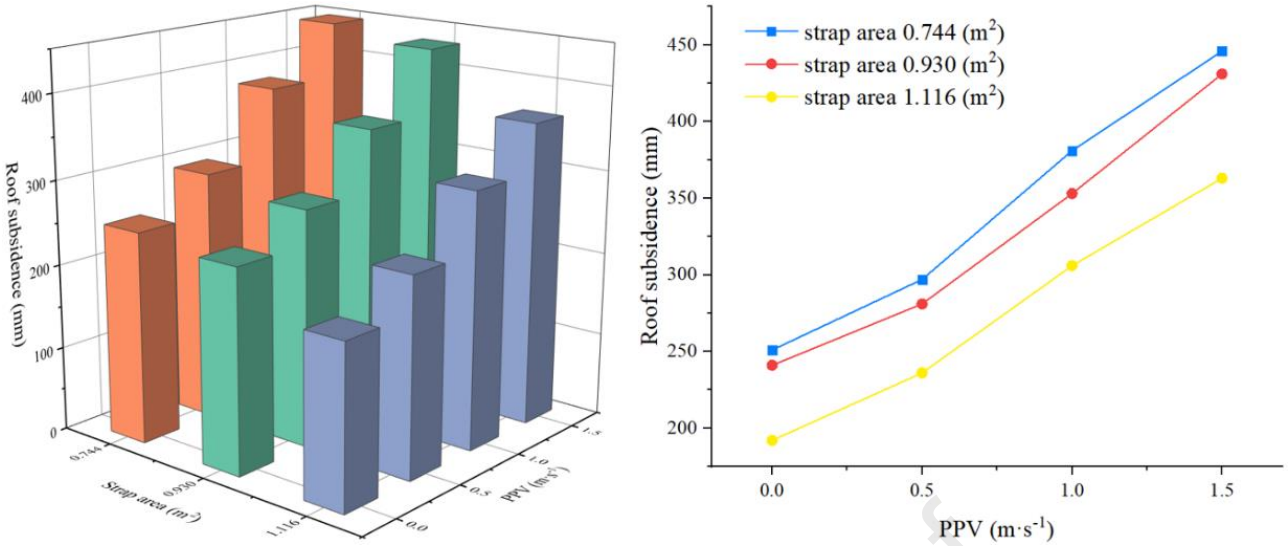

Figure 17. Roof subsidence of the roadway under different strap areas and dynamic loadings.

Similar to the analysis of the roof, Figs. 18 and 19 respectively show the horizontal displacement distribution and maximum convergence of the ribs under different working conditions. The findings indicate a positive correlation between rib convergence and dynamic loading, with rib convergence increasing as the dynamic loading intensifies. Additionally, a significant negative correlation is observed between roof subsidence and the strap area. For example, when the strap area is 0.744 m^2 and the *PPV* increases from 0 m/s to 1.5 m/s, the convergence of the ribs increases from 295.77 mm to 507.04 mm, representing a difference of 211.27 mm. Similarly, with a strap area of 1.116 m^2, the rib convergence increases from 279.34 mm to 477.86 mm, showing an increase of 198.52 mm as the *PPV* rises from 0 m/s to 1.5 m/s. The results show that under low dynamic loading (*PPV* = 0.0–0.5 m/s), increasing the SRE area can reduce the deformation of the surrounding rock, and the reduction range increases with increasing dynamic loading. However, under high dynamic loading (*PPV* = 1.0–1.5 m/s), with the exception of the scheme with a 1.116 m^2 strap, the other schemes show limited control over the rib deformation. The variation in deformation among the schemes appears to be less sensitive to dynamic loading, indicating that the impact of the SRE area on rib convergence does not significantly increase with higher dynamic loading.

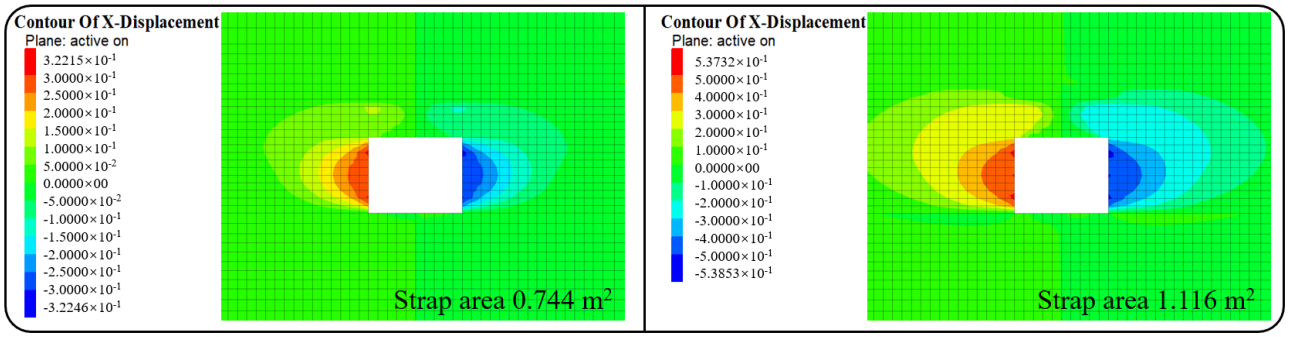

(a) PPV=0 m/s

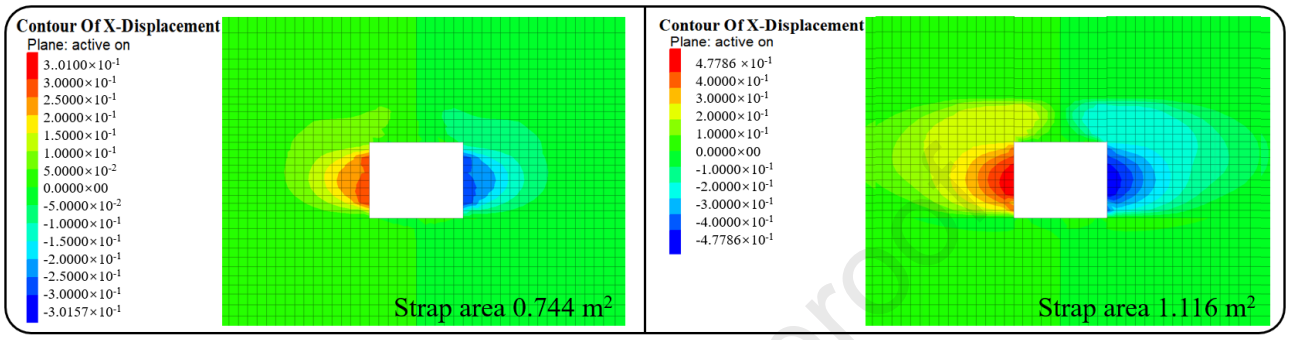

(b) PPV=1.5 m/s

Figure 18. Rib horizontal displacement distribution under different strap areas and dynamic loadings.

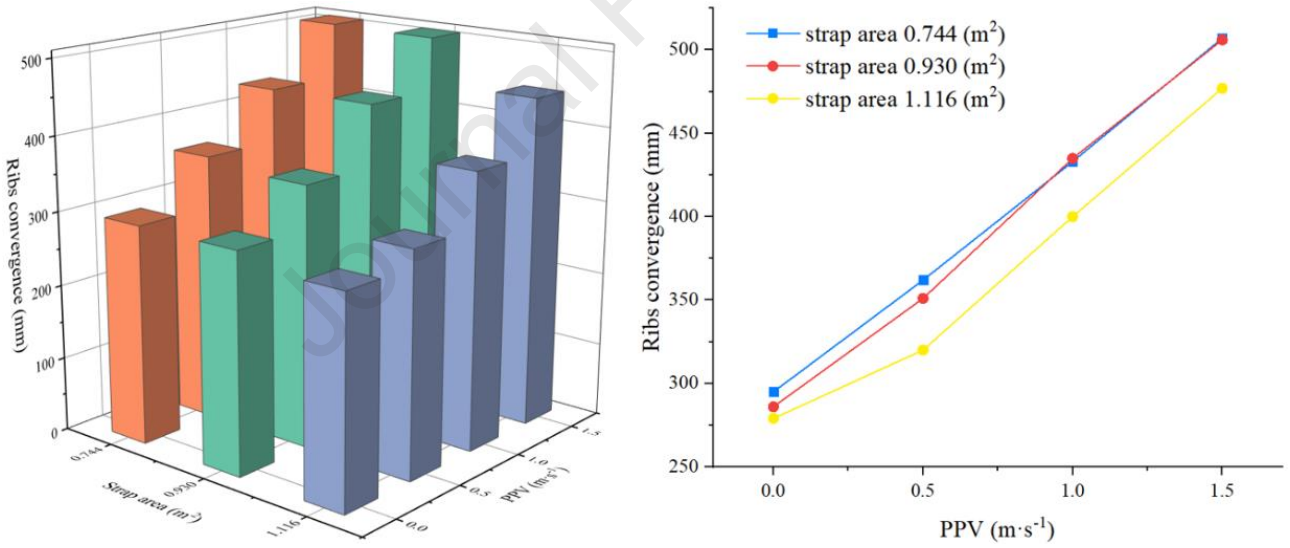

Figure 19. Rib convergence of the roadway under different strap areas and dynamic loadings.

3.3.2 Influence of the SRE area on the plastic failure of the surrounding rock under dynamic loading

After excavating the roadway, the surrounding rock is prone to plastic deformation caused by bidirectional unequal stress. Local distortion and expansion of the plastic failure zone are crucial in high-stress rock roadway instability (Fan, 2020). The distribution of the plastic failure zone in the surrounding rock is an effective indicator for assessing roadway stability. To study the effect of SRE on plastic failure in surrounding rock under dynamic loading, plastic failure zones around the roadway

were marked using the FISH module in FLAC3D. The plastic failure distribution of the surrounding rock along the axial and vertical sections of the monitoring section was obtained for each SRE area under various dynamic loadings, as depicted in Fig. 20.

From the figure, it is evident that the common characteristic of surrounding rock failure under all conditions is the wider distribution of the plastic failure zone in both the roof and the ribs. This distribution range expands as the dynamic loading increases, with the ribs showing a more pronounced effect. As shown in Fig. 20(a), when the *PPV* increases from 0 m/s to 1.5 m/s, the plastic zone range of the roof increases from 3.37 m to 4.96 m, and the ribs increase from 6.50 m to 10.44 m, representing increases of 47.18% and 60.61%, respectively. Similarly, as shown in Fig. 20(b), when the *PPV* increases from 0 m/s to 1.5 m/s, the plastic zone range of the roof increases from 3.37 m to 4.96 m, and the ribs increase from 6.00 m to 10.44 m, representing increases of 47.18% and 74.00%, respectively. Furthermore, in Fig. 20(c), as the *PPV* increases from 0 m/s to 1.5 m/s, the plastic zone range of the roof increases from 3.37 m to 3.90 m, and the ribs increase from 5.00 m to 9.60 m, resulting in a percentage increase of 15.72% and 92.00%, respectively. The results indicate that under low dynamic loading, the SRE area has minimal influence on the plastic failure zone of the surrounding rock. However, its effect on the roof becomes more pronounced with an increase in dynamic loading. A larger SRE area reduces near-field surrounding rock plastic failure and delays the expansion of the plastic failure zone.

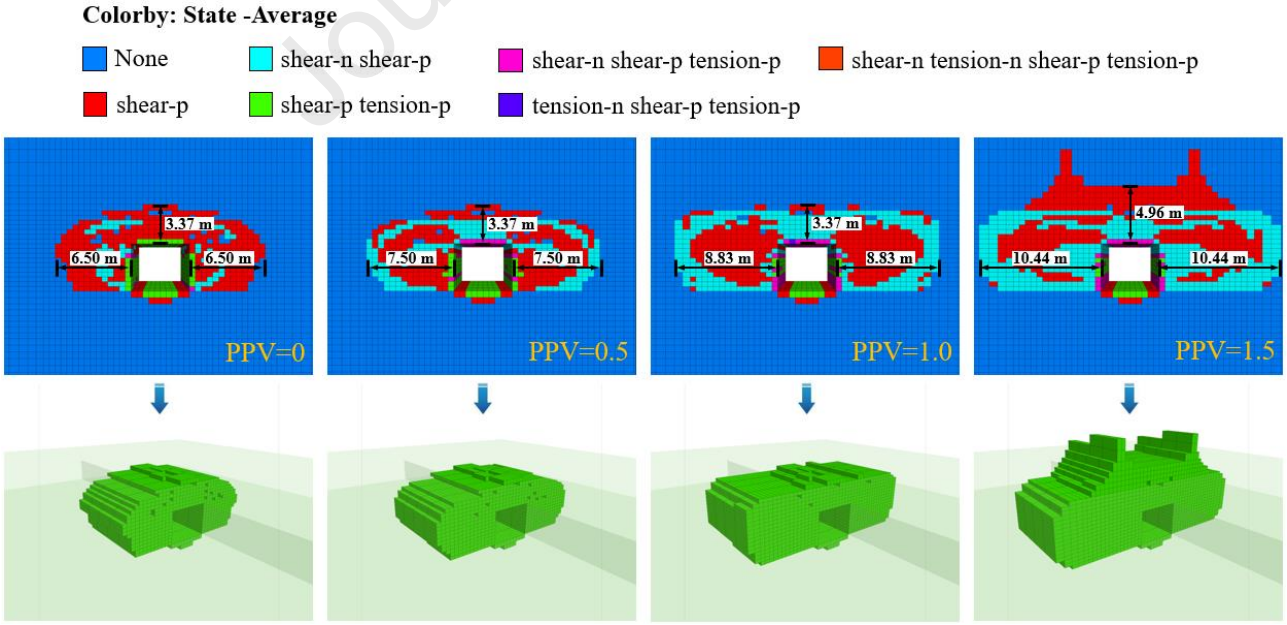

(a) Strap area 0.744 m^2

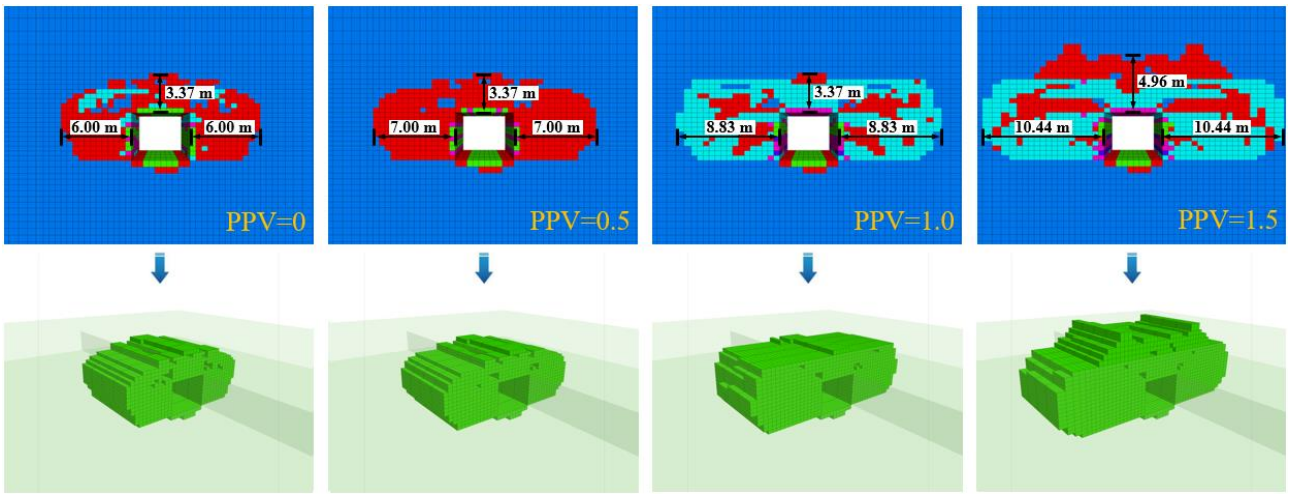

(b) Strap area 0.930 m^2

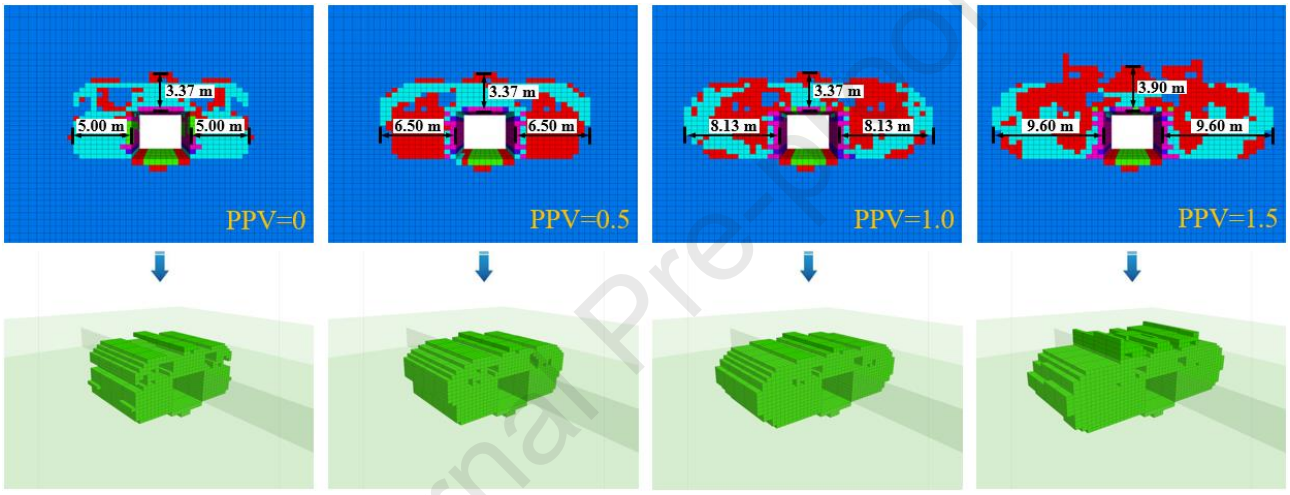

(c) Strap area 1.116 m^2

Figure 20. Distribution of roadway plastic failure under different strap areas and dynamic loadings.

To further analyze the failure characteristics of the roadway under different SRE areas and dynamic loadings, the plastic failure zones obtained using the FISH language and the total number of surrounding rock zones in the near-field roadway were extracted (Table 8). The ratio of the two was defined as the plastic failure ratio, as illustrated in Fig. 21. The plastic failure ratio of surrounding rock increases with *PPV* but decreases with strap area. For instance, when the *PPV* is 0 m/s, the plastic failure ratio of the surrounding rock decreases by 5.6% from 34.1% to 28.5% as the surface area of the strap increases from 0.744 m^2 to 1.116 m^2. Similarly, when the *PPV* is 1.5 m/s, the plastic failure ratio of the surrounding rock decreases by 23.2% from 75.4% to 52.2% as the surface area of the strap increases from 0.744 m^2 to 1.116 m^2. The results show that the plastic failure ratio of surrounding rock correlates with dynamic loading strength, with a decreasing growth rate as SRE area increases. Notably, the strap with an area of 1.116 m^2 exhibits a more pronounced inhibitory effect on the plastic

failure of the surrounding rock and exerts a more significant control effect on the surrounding rock under strong dynamic loading.

Table 8 Roadway plastic failure zone under different SREs and dynamic loadings.

	Strap area 0.744 m^2	Strap area 0.930 m^2	Strap area 1.116 m^2	Zone of near-field roadway
PPV 0.0 m/s	1703	1593	1427	4992
PPV 0.5 m/s	2031	1871	1778	
PPV 1.0 m/s	2576	2426	2146	
PPV 1.5 m/s	3386	3255	2606	

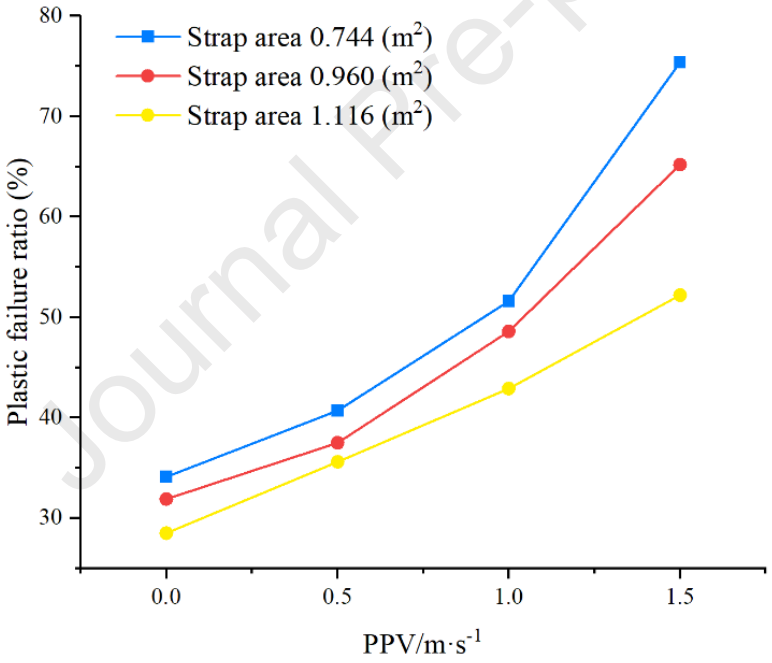

Figure 21. Roadway plastic failure ratio under different strap areas and dynamic loadings.

4. Discussion

The rock support system operates in accordance with the principle of the weakest link, which means that the overall stability of the support system depends on the weakest internal support element. This principle assumes particular significance when roadways are subjected to complex conditions, especially those involving high stress and significant dynamic loads (Stacey, 2011). In roadways prone to frequent dynamic disasters such as rockbursts, the support system must not only consider

static load-bearing capacity but also incorporate dynamic load energy absorption characteristics. A comprehensive understanding of the functions performed by each support element within the system, along with careful selection of suitable combinations, is crucial in designing an effective and robust support system. Within the realm of dynamic loads, the bolt initially undergoes yielding to absorb energy, while the SRE resists premature failure, subsequently demonstrating its potential to absorb energy during the dynamic loading process. This enhances the energy-absorption ability of rock bolts. In instances where the rock mass remains intact and robust, a significant portion of the energy is absorbed by the bolt. Conversely, when the rock mass is fractured and weakened, the SRE assumes a more significant role in energy absorption. The amount of energy absorbed by these elements depends on factors such as the type, stiffness, mechanical properties of the surrounding rock, and intensity of the dynamic loading stress wave (Geobrugg, 2013). Simultaneously, the fracturing of the surrounding rock itself contributes to the dissipation of a portion of energy (W_f). To prevent rockburst incidents, it is crucial that the support system absorbs more cumulative energy (W_{rs}) than the residual energy released after rock rupture. This means the following:

$$W_{rs} \geq W - W_f \tag{4}$$

For a given total released energy, W, the efficient dissipation of energy through rock fracture can significantly decrease the energy that needs to be absorbed by the support system. While most rockbursts occur in hard and brittle rock formations within high-stress environments, this highlights the significance of prioritizing the energy absorption characteristics of bolts. Notably, recent studies have indicated that enhancing the capabilities of the SRE not only improves the overall energy absorption characteristics of the support system but also contributes to enhanced energy dissipation within the rock itself (Li, 2021). In the realm of current and future ground support strategies, the primary objective will be to achieve stable reinforcement for surrounding rock in challenging scenarios, such as those involving "three heights and one disturbance." Additionally, significant attention will be given to addressing substantial structural deformations. This objective will be achieved by synergistically integrating the bolt-SRE system with surrounding rock reinforcement.

In deep roadway support design, the utilization of high-strength rock bolts, high-strength energy-absorbing SREs, and grouting reinforcement measures constitutes a primary strategy for mitigating dynamic disaster risks. The energy absorption capabilities of support elements under different geological conditions are analyzed to optimize key parameters such as bolt yield strength, SRE

stiffness, and structural ductility. By quantifying these contributions, the goal is to ensure synergistic compatibility between support materials and the mechanical behavior of the surrounding rock, thereby improving overall stability and performance. While enhanced energy absorption characteristics improve safety, they concurrently elevate costs. Consequently, support system design necessitates equilibrium between safety requirements and cost-effectiveness. Strategic selection of bolt types, lengths, and densities, combined with material optimization and dimensional control of SREs, enables cost reduction without surrounding rock integrity. In addition, "main energy absorption zone" and "secondary energy absorption zone" can be divided according to the integrity of surrounding rock, dynamic load risk level and energy release intensity. The main energy absorption zone gives priority to high-energy SREs, and the secondary energy absorption zone is dominated by high-strength bolts, so as to realize the energy guidance and dissipation path design in space. With the development of material science, new supporting materials and structures will also provide more choices for the design of ground supporting systems.

5. Conclusion

(1) Under dynamic loading, the dynamic strength and modulus of elasticity of bolted specimens increase with increasing SRE area, and they are positively correlated. At the same time, increasing the surface area of the SRE can improve the dissipation of energy in the specimens during impact and enhance the ability of the bolted specimens under dynamic loadings.

(2) The continuous action of stress waves of dynamic loading increases the lateral constraints on the specimens by the SREs. As a result, the bolt and the specimens become more inclined toward codeformation. The utilization of a larger surface area of SREs is beneficial for delaying the initiation of cracks, minimizing crack propagation, and improving the structural integrity of fragments following impact failure.

(3) After applying dynamic loading to the numerical model, the SRE significantly influences the roof. For the ribs, increasing the SRE area can significantly reduce the deformation of the surrounding rock under low dynamic loading. However, under high dynamic loading, the control effect of the SRE on the ribs is not significant. Second, increasing the SRE area of the protector helps to minimize plastic failure in the near-field surrounding rock and delay the expansion of the plastic zone.

(4) Under the conditions of static and dynamic load superposition, the comprehensive and

systematic support of the roadway is a prerequisite for its support design. The design should not only focus on enhancing the performance of the bolt itself but also consider the significance of other supporting elements, such as SREs. It is important to carefully select the coordination relationship between support technology and elements to minimize the likelihood of dynamic disasters.

Acknowledgements

This study was financially supported by the Young Scientist Project of National Key Research and Development Program of China (2021YFC2900600), the National Natural Science Foundation of China (52074166) and Shandong Province (ZR2021YQ38).

References

Dan, R.L., Peng, Y.H., Kong, X.S., Xiao, Y.H., Yuan, H.H., Huang, B., Zheng, Y., 2019. Research progress of coal roadway support technology at home and abroad. Chinese Journal of Rock Mechanics and Engineering 8(12):2377–2403. https://doi.org/10.13722/j.cnki.jrme.2019.0386

Fu, Y.K., Sun, Z.Y., Ju, W.J., 2019. Response and impact mechanism of rock bolt under lateral dynamic impact load. Journal of China Coal Society 44(07):2020–2029. https://doi.org/10.13225/j.cnki.jccs.2015.1618

Fan, D., Liu, X., Tan, Y., Li, X., Yang, S., 2024. Energy mechanism of bolt supporting effect to fissured rock under static and dynamic loads in deep coal mines. International Journal of Mining Science and Technology, 34(3), 371–384.

Fan, L., Wang, W.J., Yuan, C., Peng, W.Q., 2020. Research on large deformation mechanism of deep roadway with dynamic pressure. Energy Science & Engineering 8(9). https://doi.org/10.1002/ese3.672

Fedrizzi, R.M., Ceia, M., Misságia, R.M., Santos, V.H., Neto, L.I., 2018. Artificial carbonate rocks: Synthesis and petrophysical characterization. Journal of Petroleum ence & Engineerin 163:303-310. https://doi.org/10.1016/j.petrol.2017.12.089

Feng, P., Zhao, J., Dai, F., Wei, M.D., Liu, B., 2022a. Mechanical behaviors of conjugate-flawed rocks subjected to coupled static–dynamic compression. Acta Geotechnica, 17(5), 1765-1784.

Feng, P., Liu, B., Tang, R., Wei, M., Zhang, Y., Li, H., 2022b. Dynamic fracture behaviors and fragment characteristics of pre-compressed flawed sandstones. International Journal of Mechanical Sciences, 220, 107162.

Ferrero, A.M., 1995. The shear strength of reinforced rock joints. International Journal of Rock

Mechanics & Mining Sciences & Geomechanics Abstracts 32(6):595-605. https://doi.org/10.1016/0148-9062(95)00002-X

Geobrugg, R.B., Zimmermann, A., Ag, G., Solutions, G., Cala, M., 2013. Large scale field tests of high-tensile steel wire mesh in combination with dynamic rockbolts subjected to rockburst loading. In: Proceedings of the Seventh International Symposium on Ground Support in Mining and Underground Construction, Australian Centre for Geomechanics, Perth, 221–232.

Gell, E.M., Walley, S.M., Braithwaite, C.H., 2019. Review of the validity of the use of artificial specimens for characterizing the mechanical properties of rocks. Rock Mechanics and Rock Engineering 52(9). https://doi.org/10.1007/s00603-019-01787-8

He, J., Wu, Y.Z., Fu, Y.K., 2021. Mechanics response law of surface protecting components for rock bolting under impact load. Journal of Mining & Safety Engineering 38(3):9. https://doi.org/10.13545/j.cnki.jmse.2020.0538

Hadjigeorgiou, J., Potvin, Y., 2011. A critical assessment of dynamic rock reinforcement and support testing facilities. Rock mechanics and rock engineering 44: 565–578. https://doi.org/10.1007/s00603-011-0155-4

Han, Z.Y., Li, D.Y., Zhou, T., Chen, J.R., Xie, S.J., 2022. Dynamic progressive fracture behavior of axially confined sandstone specimens containing a single flaw. Theoretical and Applied Fracture Mechanics 122:103597. https://doi.org/10.1016/j.tafmec.2022.103597

Ivars, D.M., Pierce, M.E., Darcel, C., Reyes-Montes, J., Potyondy, D.O., Young, R.P., Cundall, P.A., 2011. The synthetic rock mass approach for jointed rock mass modelling. International Journal of Rock Mechanics and Mining Sciences 48:219–244. https://doi.org/10.1016/j.ijrmms.2010.11.014

Jiang, L.S., Wu, X.Y., Wang, Q.W., Feng, H., Wu, Q.H., 2021. Dynamic mechanical behaviors of sand-powder #D printing rock-like specimens under coupled static and dynamic loads. Journal of China Coal Society 47(03): 1196–1207. https://doi.org/10.13225/j.cnki.jccs.xr21.1529.

Kang, H.P., Gao, F.Q., Xu, G., Ren, H., 2023. Mechanical behaviors of coal measures and ground control technologies for China's deep coal mines e A review. Journal of Rock Mechanics and Geotechnical Engineering 15(1):37–65. https://doi.org/10.1016/j.jrmge.2022.11.004

Khoshmagham, A., Shirinabadi, R., Tabrizi, A.H.B., Gholinejad, M., Kianoush, P., 2025. Exploring the time-dependent behaviors of the rock mass roof of tunnels in open underground spaces of coal mines through numerical investigation. Scientific Reports, 15(1), 8703.

Li, C.C., 2017. Principles of rockbolting design. Journal of Rock Mechanics and Geotechnical Engineering 9(3):19. https://doi.org/10.1016/j.jrmge.2017.04.002

Li, D., Gao, F., Han, Z., Zhu, Q., 2020. Experimental evaluation on rock failure mechanism with combined flaws in a connected geometry under coupled static-dynamic loads. Soil Dyn Earthq Eng 132: 106088.

Li, G., Hu, Y., Tian, S.M., Ma, W.B., Hang, H.L., 2021. Analysis of deformation control mechanism of prestressed anchor on jointed soft rock in large cross-section tunnel. Bulletin of Engineering Geology and the Environment 80(12):9089–9103. https://doi.org/10.1007/s10064-021-02470-5

Li, C.C., 2021. Principles and methods of rock support for rockburst control. Journal of Rock Mechanics and Geotechnical Engineering 13(1):14. https://doi.org/10.1016/j.jrmge.2020.11.001

Louchnikov, V.N., Eremenko, V.A., Sandy, M.P., Kosyreva, M.A., 2017. Support Design for Mines Exposed to Rockburst Hazard. Journal of Mining Science 53(3):86–95. https://doi.org/10.1134/S1062739117032439

Primkulov, B., Chalaturnyk, J., Chalaturnyk, R., Zambrano-Narvaez, G., 2017. 3d printed sandstone strength: curing of furfuryl alcohol resin-based sandstones. 3D Printing and Additive Manufacturing 4(3):149–155. https://doi.org/10.1089/3dp.2017.0032

Qiu, P.Q., Ning, J.G., Wang, J., Yang, S., Hu, S.C., Tan, Y.L., Wei, X., Yan, S.S., 2020. Experimental study on impact resistance timeliness of bolted rock under dynamic load. Journal of China Coal Society 37(01):50–61. https://doi.org/11.2190.TD.20201025.1115.001

Qiu, P.Q., Wang, W.W., Wang, K., Ning, J.G., Zhang, X.Q., Zhao, C.L., Cai, T.T., 2025. Experimental Investigation of the Dynamic Impact Failure of Bolted Rock with Different Anchoring Angles. Energy Science & Engineering 13(2): 752–764. https://doi.org/10.1002/ese3.2032

Stacey, T.R. (2011. A philosophical view on the testing of rock support for rockburst conditions. Journal- South African Institute of Mining and Metallurgy 112(8):01–08.

Smith, S.E., MacLaughlin, M.M., Adams, S.L., Wartman, J., Applegate, K., Gibson, M., Arnold, L., Keefer, D., 2014. Interface properties of synthetic rock specimens: experimental and numerical investigation. Geotech Test J 37(5). https://doi.org/10.1520/GTJ20130161

Sakurai, S., 2010. Modeling strategy for jointed rock masses reinforced by rock bolts in tunneling practice. Acta Geotechnica 5(2):121–126. https://doi.org/10.1007/s11440-010-0117-0

Tian, W., Han, N.V., 2017. Mechanical properties of rock specimens containing pre-existing flaws with 3d printed materials. Strain 53(6). https://doi.org/10.1111/str.12240

Villaescusa, E., Thompson, A., Player, J., 2015. Dynamic testing of ground support systems. Minerals Research Institute of Western Australia. https://doi.org/10.13140/RG.2.1.5047.4962

Vogler, D., Walsh, S., Dombrovski, E., Perras, M.A., 2017. A comparison of tensile failure in 3d-printed and natural sandstone. Engineering Geology 226:221–235. https://doi.org/10.1016/j.enggeo.2017.06.011

Wu, B., Yao, W., Xia, K., 2016. An experimental study of dynamic tensile failure of rocks subjected to hydrostatic confinement. Rock Mechanics & Rock Engineering 49(10):1–10. https://doi.org/10.1007/s00603-016-0946-8

Wu, X., Jiang, L., Tao, M., Hani, S.M., Xiang, G.L., 2024. Dynamic behaviors and bolt-strengthening effect of sand-powder 3D printing rock analog under static and dynamic coupled loading. Construction and Building Materials, 411, 134723.

Xie, H.P., Gao, M.Z., Zhang, R., Peng, G.Y., Wang, W.Y., Li, A.Q., 2019. Study on the Mechanical Properties and Mechanical Response of Coal Mining at 1000m or Deeper. Rock Mechanics and Rock Engineering 52:1–16. https://doi.org/10.1007/s00603-018-1509-y

Xu, R.C., Zhou, H., 2019. Experimental investigation of the anchoring effect of two different types of rock bolts on fractured rock. Advances in Materials Science and Engineering (3):1–10. https://doi.org/10.1155/2019/9290318

Xu, X.G., Feng, H., Jiang, L.S., Guo, T., Wu, X.Y., Sun, Z.Q., 2021. Research on Deformation and Failure Evolution of Deep Rock Burst Drivage Roadway Surrounding Rock under Dynamic loading. Shock and Vibration 1–13. https://doi.org/10.1155/2021/7956421

Zhu, W., Jing, H., Yang, L., Pan, B., Su, H., 2018. Strength and deformation behaviors of bedded rock mass under bolt reinforcement. International Journal of Mining Science and Technology 28(4): 593–599. https://doi.org/10.3969/j.issn.2095-2686.2018.04.005

Highlights

1. The mechanical behaviors of 3D-printed rock exhibited similarities to soft rock, validating their applicability in rock mechanics research.
2. Enhancing the area of surface retaining element (SRE) can effectively improve the dynamic mechanical behaviors and integrity of the bolted specimen.
3. SREs demonstrated a more pronounced inhibitory effect on plastic failure in roadway surrounding rock under intense dynamic load disturbances.

Declaration of interests

☒ The authors declare that they have no known competing financial interests or personal relationships that could have appeared to influence the work reported in this paper.

☐The authors declare the following financial interests/personal relationships which may be considered as potential competing interests: